Lagged effects regulate the inter-annual variability of the tropical carbon balance

A. Anthony Bloom[1], Kevin W. Bowman[1], Junjie Liu[1], Alexandra G. Konings[2], John R. Worden[1], Nicholas C, Parazoo[1], Victoria Meyer[1], John T. Reager[1], Helen M. Worden[5], Zhe Jiang[6], Gregory R. Quetin[2], T. Luke Smallman[3,4], Jean-François Exbrayat[3,4], Yi Yin[1], Sassan S. Saatchi[1], Mathew Williams[3,4], David S. Schimel[1].

[1]Jet Propulsion Laboratory, California Institute of Technology, Pasadena, CA 91101, U.S.A.
[2]Department of Earth System Science, Stanford University, Stanford, CA 94305, U.S.A.
[3]School of Geosciences, University of Edinburgh, Edinburgh, EH9 3FF, United Kingdom.
[4]National Centre for Earth Observation, Edinburgh EH9 3FF, United Kingdom.
[5]National Center for Atmospheric Research, Boulder, 80301 CO, U.S.A.
[6] School of Earth and Space Sciences, University of Science and Technology of China, Hefei, 230026, China.

Correspondence to: A. Anthony Bloom (abloom@jpl.nasa.gov)

Abstract.

Inter-annual variations in the tropical land carbon (C) balance are a dominant component of the global atmospheric CO_2 growth rate. Currently, the lack of quantitative knowledge on processes controlling net tropical ecosystems C balance on inter-annual timescales inhibits accurate understanding and projections of land-atmosphere C exchanges. In particular, uncertainty on the relative contribution of ecosystem C fluxes attributable to concurrent forcing anomalies (concurrent effects) and those attributable to the continuing influence of past phenomena (lagged effects) stifles efforts to explicitly understand the integrated sensitivity of tropical ecosystem to climatic variability. Here we present a conceptual framework—applicable in principle to any land biosphere model—to explicitly quantify net biospheric exchange (*NBE*) as the sum of anomaly-induced concurrent changes and climatology-induced lagged changes to terrestrial ecosystem C states ($NBE = NBE^{CON} + NBE^{LAG}$). We apply this framework to an observation-constrained analysis of the 2001-2015 tropical C balance: we use a data-model integration approach (CARDAMOM) to merge satellite-retrieved land-surface C observations (leaf area, biomass, solar-induced fluorescence), soil C inventory data and satellite-based atmospheric inversion estimates of CO_2 and CO fluxes to produce a data-constrained analysis of the 2001-2015 tropical C cycle. We find that the inter-annual variability of both concurrent and lagged effects substantially contribute to the 2001-2015 NBE inter-annual variability throughout 2001-2015 across the tropics (NBE^{CON} IAV = 80% of total *NBE* IAV, r = 0.76; NBE^{LAG} IAV = 64% of *NBE* IAV, r = 0.61) and the prominence of NBE^{LAG} IAV persists across both wet and dry tropical ecosystems. The magnitude of lagged effect variations on *NBE* across the tropics is largely attributable to lagged effects on net primary productivity (*NPP*; NPP^{LAG} IAV 113% of NBE^{LAG} IAV, r = -0.93, p-value<0.05), which emerge due to the dependence of *NPP* on inter-annual variations in foliar C and plant-available H_2O states.

We conclude that concurrent and lagged effects need to be explicitly and jointly resolved to retrieve an accurate understanding the processes regulating the present-day and future trajectory of the terrestrial land C sink.

1 Introduction

Immediate ecosystem responses to external forcings are invariably followed by time-lagged ecosystem responses, attributable to a continuum of lagged biotic and physical processes. For example, contemporaneous ecosystem state changes attributable to disturbances, climatic variability and increasing atmospheric CO_2 levels all induce a temporal spectrum of lagged processes, such as diurnal to seasonal dynamics in canopy and groundwater storage, multi-annual changes in mortality rates, and induce ecosystem dynamics relating to species distributions, nutrient availability and soil properties on timescales spanning from decades to millennia (Schimel et al. 1997; Smith et al., 2009; Reichstein et al., 2013). Conversely, for a given timespan, the sum of these "lagged effects" on ecosystem states ultimately represent the ecosystems dynamics attributable to a unique integrated legacy of past phenomena, spanning from diurnal to geologic timescales, making lagged effects a ubiquitous dynamical property of any terrestrial ecosystem. As a consequence, ecosystem function at any given time (such as photosynthetic uptake, respiration and evapotranspiration rates) is an emergent consequence of an ecosystem's initial physical and biotic states and the contemporaneous impact of meteorological and disturbance forcings on these states.

Disentangling the cumulative lagged consequences of past phenomena from contemporaneous impacts of external forcings is a critical priority for understanding and quantifying the contemporary terrestrial carbon (C) cycle responses to climatic variability. Global-scale efforts to resolve the state of the C cycle (Le Quéré et al., 2015) identify tropical C cycle as a dominant contributor to the inter-annual variability (IAV) of the terrestrial C sink. Recent efforts to characterize the tropical C sink IAV have been largely focused on quantifying the role of concurrent responses to climatic variability, including the contribution of semi-arid ecosystems (Poulter et al., 2014; Ahlstrom et al., 2015), ecosystem responses to drought (Gatti et al., 2014), and more generally continental-scale sensitivities of photosynthesis, respiration and fire fluxes to concurrent temperature and precipitation anomalies (Cox et al., 2013; Andela and van der Werf, 2014; Alden et al., 2016; Jung et al., 2017; Liu et al, 2017; Piao et al., 2019). However, on comparable timescales, time-lagged manifestations of climatic variability on the state of the terrestrial biosphere have been extensively theorized and observed (Thomson et al., 1996; Schimel et al., 1996, 2005; Richardson et al., 2007; Arnone et al., 2008; Sherry et al., 2008; Saatchi et al., 2013; Frank et al., 2015; Doughty et al., 2015; Baldocchi et al., 2017; Schwalm et al. 2017; amongst many others). Specifically, lagged relationships between climate variability and the terrestrial C fluxes—namely mediated through lagged impacts on photosynthetic uptake and respiration fluxes, groundwater storage, mortality and subsequent shifts of ecosystem function—indicate that lagged effects may be a fundamental component in the inter-annual evolution of the terrestrial C balance. Observational constraints on terrestrial ecosystem responses to climatic variability further suggest that time-lagged phenomena are a non-negligible component of

terrestrial ecosystem C dynamics on continental-to-global scales (Braswell et al., 1997; Saatchi et al., 2013; Anderegg et al., 2015; Detmers et al., 2015; Fang et al. 2017; Yang et al., 2018; Yin et al., 2020). Therefore, while recent efforts to diagnose inter-annual variations of the tropical C balance overwhelmingly emphasize the roles of concurrent forcings, observed ecosystems responses to climatic variability on multi-annual timescales indicate that the tropical C balance may be substantially affected—if not governed—by lagged responses to inter-annual variations in meteorological and disturbance forcings across tropical ecosystems.

Accurate knowledge of both instantaneous sensitivities and time-lagged processes of terrestrial C cycling to climate is critical for constraining model representations of the terrestrial C cycle. Uncertainty in the long-term terrestrial C flux imbalance and the associated carbon-climate feedbacks is a prevailing source of uncertainty in Earth System projections (Friedlingstein et al., 2014, Friend et al., 2014), and these are likely underestimated due to a range of under-represented and/or poorly constrained C cycle responses to a changing climate (Luo 2007; Lovenduski & Bonan, 2017). Furthermore, assessments of Earth System projections based on present-day constraints (Cox et al., 2013; Mystakidis et al., 2016) provide little insight on the integrated roles of largely uncertain process controls, including C flux responses to drought (Powell et al., 2013); under-determined C pool dynamics (Bloom et al., 2016), nutrients dynamics and limitations (Wieder et al., 2015), and higher-order dead organic C dynamics (Schimel et al., 1994, Hopkins et al., 2014). In tropical ecosystems, rapid turnover rates of live and dead organic matter pools, relative to extra-tropical ecosystems (Carvalhais et al., 2014; Bloom et al., 2016) imply interactions between uptake, respiration, and fires (Randerson et al., 2005; Chen et al., 2013, Bloom et al., 2015) on comparable timescales: specifically, given that (a) the mean C residence time in tropical biomass and soil organic matter pools typically spans ~5-50 years, and (b) multi-year observational constraints reveal rapid ecosystem vegetation/C responses to climatic extremes (Saatchi et al., 2013; Alden et al., 2016), sub-decadal timescales are likely critical for disentangling concurrent and lagged effect impacts on the evolution of tropical C balance. However, despite numerous studies on the roles of productivity (Doughty et al., 2015), water stress (Kurc & Small, 2007; Williams & Albertson, 2004), respiration (Trumbore 2006, Exbrayat et al 2013a,b, Guenet et al., 2018) and mortality (Saatchi et al., 2013, Anderegg et al., 2015; Rowland et al., 2015), there is currently a major gap between knowledge of individual processes controlling the tropical C balance on inter-annual timescales, and the integrated impact process interactions leading to complex net C exchanges represented in terrestrial biosphere models (Huntzinger et al., 2013, 2017). As a result, while models provide critical mechanistic insight into complex process interactions, model representations of the net effect of competing and interacting C flux responses to climate variability and disturbance remain highly uncertain on regional and pan-tropical scales. Ultimately, given tropical ecosystems account for 850 Pg of C and the majority of the Earth's photosynthetic uptake, plant respiration and fire C emissions (Saatchi et al., 2011; Hiederer & Köchy, 2011; Beer et al., 2010; van der Werf et al., 2010), quantitatively understanding the concurrent and long-lived impacts of climatic variability, drought and anthropogenic disturbance is critical for predicting their function in Earth system projections.

Recent inverse estimates of tropical C fluxes from satellite CO_2 measurements provide much-needed spatial and temporal constraints on continental-scale Net Biospheric Exchange (NBE; e.g. Takagi et al., 2014, Liu et al., 2014, 2017; Feng et al., 2017., Detmers et al., 2015; amongst others). Satellite-based NBE estimates—combined with land-surface observations of solar-induced fluorescence (SIF, Frankenberg et al. 2011), leaf-to-soil constraints on total C stocks (Saatchi et al., 2011) and disturbance (Giglio et al., 2013)—provide a unique opportunity for quantitatively informing terrestrial biosphere model representations of the tropical C balance; recent continental-to-global scale model-data fusion efforts have demonstrated the synergistic potential of the present-day "carbon observing system" for resolving the dynamics of the terrestrial C balance (Liu et al., 2017; Bloom et al. 2016; MacBean et al., 2018; Exbrayat et al. 2018; Quetin et al., 2020; Yin et al., 2020). Ultimately, model-data fusion representations of terrestrial ecosystem C cycling allow for an explicitly mechanistic representation of the terrestrial C balance with in-built states and process parametrizations optimized to represent the observed C cycle variability in the observations; contingent on their mechanistic accuracy of the C cycle to external forcings, these terrestrial C balance models can be used to quantitatively diagnose the concurrent and lagged sensitivities of terrestrial ecosystems to external forcings.

In this study we present a framework for expressing the ecosystem state changes in a given year as the sum of (a) "concurrent effects", attributable to concurrent forcing anomalies, and (b) "lagged effects", attributable to the cumulative impacts of past forcings. We apply this framework on a data-constrained ecosystem C balance modelling framework to quantitatively diagnose the role of concurrent and lagged effects on the 2001-2015 inter-annual tropical C balance. Our analysis is motivated by some key unanswered questions on the large-scale tropical C cycle variability: for instance, are lagged effects significant contributors to inter-annual flux variability on pan-tropical scales? Which C fluxes (e.g. photosynthetic or respiratory) explain the majority of NBE variability attributable to lagged phenomena? Are lagged effects a ubiquitous property across both dry and wet tropical biomes? Here we hypothesize that on a pan-tropical scale, the integrated impact of lagged effects is a critical component of tropical NBE IAV. To test this hypothesis, we reconcile large-scale C cycle processes and satellite-based estimates of land-to-atmosphere CO_2 fluxes using the CARDAMOM diagnostic ecosystem C balance model-data fusion approach. We outline our method in section 2, where we present an analytical methodology for attributing inter-annual ecosystem state variability to concurrent and lagged effects; we present and discuss a quantification of the relative role of concurrent and lagged effects on continental-scale NBE, and the attribution of lagged effects to inter-annual variations in C stock and plant-available water states in section 3; we conclude our manuscript in section 4.

2 Methods

To quantitatively diagnose concurrent and lagged effects on the inter-annual variability of the tropical C balance, we (i) present a conceptual framework for attributing annual ecosystem state changes to concurrent and lagged components, (ii) implement CARDAMOM model-data fusion framework at a 4°×5° monthly resolution to observationally constrain 2001-2015 C cycle

states, fluxes and process controls, and (iii) attribute ecosystem state changes to concurrent and lagged effects based on the CARDAMOM 2001-2015 representation of the tropical C balance. In summary, the CARDAMOM model-data fusion framework (Bloom et al., 2016) employs a Bayesian inference approach to constrain model parameters and initial states within the prognostic Data Assimilation Linked Ecosystem Carbon model (DALEC, Williams et al., 2005), based on observation constraints—where and when these are available. Since DALEC parameters are independently estimated at each location, the 4°×5° resolution was chosen to accommodate recent estimates of land-surface CO_2 and CO fluxes produced at the GEOS-Chem atmospheric chemistry and transport model 4°×5° grid (Bowman et al., 2017; Liu et al. 2017; Jiang et al., 2017). We implement the CARDAMOM analysis across tropical and near-tropical latitudes (30°S - 30°N), and evaluate the tropical C balance across 6 sub-continental regions, as well as the dry tropics and the wet tropics (Figure A1); we chose to focus the evaluation of our results at sub-continental and pan-tropical scales to conform with the fundamental spatial resolution limitations of satellite-based surface CO_2 flux estimates (Liu et al., 2014, Bowman et al., 2017). The following subsections describe a conceptual framework for concurrent and lagged effect attribution (2.1), the DALEC ecosystem carbon balance model (2.2), satellite and inventory-based observations (2.3), the estimation of DALEC parameters and states within the CARDAMOM model-data fusion framework (2.4), and the attribution of the observation-informed DALEC C cycle dynamics to their concurrent and lagged effect components (2.5).

2.1 Concurrent and lagged effects

Ecosystem function—such as photosynthesis, respiration and evapotranspiration rates—at all stages of ecological succession is both a consequence of an ecosystem's initial physical and biotic states and the contemporaneous impact of meteorological and disturbance forcings on these states. For example, ecosystem water and nutrient availability along with species demography and species composition—effectively amounting to the time-integrated ecosystem legacy—will govern an ecosystem's function under a nominal forcing. The cumulative impact of both episodic or prolonged variability in external forcings will be "remembered" in ecosystem states, thus shaping ecosystem function as an emergent property of external forcing history. Ecosystem states under a constant and perpetual environmental forcing will follow a trajectory towards an equilibrium state (as has been largely hypothesized as the typical outcome for ecosystem C stocks; Luo and Weng 2011, Luo et al. 2015) or more generally a transient trajectory about a domain of attraction (Holling, 1973), with stable equilibria, stable limit cycles, stable nodes and/or neutrally stable orbits as potential trajectories. Here, we define *lagged effects* as the sum of ecosystem state changes induced by a reference climatological mean forcing (Figure 1); these include the functional responses of ecosystem under climatological conditions (e.g. joint photosynthesis, respiration and evapotranspiration responses to non-equilibrium plant-available water, leaf area, biomass and dead organic C states), as well as functional shifts (e.g. succession-induced changes in demography and species composition, and consequently changes in ecosystem-scale photosynthetic capacity). In addition to an attraction towards a fixed equilibrium or domain, ecosystem states are perpetually disturbed by exogenous forces, such as meteorological and disturbance forcing anomalies relative to a climatological mean forcing. Here

we define these *concurrent effects* as all anomaly-concurrent changes to ecosystem states unaccounted for by climatology-induced state changes (i.e. *lagged effects*); these include functional responses to anomalous forcings (e.g. drought impact on photosynthetic uptake and respiration in responses to meteorological phenomena), as well as functional shifts on demographics and species composition induced by concurrent mortality and disturbance events. The combined state changes resulting from both concurrent and lagged effects throughout a one-year time period will in turn propagate into future ecosystem states. In this manner, forcing anomalies are perpetually propagated into ecosystem states, and lagged effects in subsequent years represent an aggregate legacy of all prior phenomena. The choices of (a) "concurrent effects" to describe effects contemporaneous to a meteorological event and (b) "lagged effects" to describe all time-lagged processes are consistent with Frank et al., (2015) definitions associated with effects occurring during or after a climatic anomaly. We note a distinction between (i) single-event lagged effects, which represent ecosystem state changes attributable to a single past forcing event (ii) aggregate lagged effects, which represent the sum and interactions between past single-event lagged effects. For example, single-event lagged effects might include the ecosystem state changes attributable to a single drought or disturbance event, while aggregate lagged effects can include the effects of cumulative droughts impacts, the interactions in between dry and wet year events, and the longer-term succession processes (as described in Figure 1); we henceforth use "lagged effects" to refer to aggregate lagged effects throughout the manuscript. Finally, while in this study we confine our analysis to the estimation of concurrent and lagged effects on annual timescales, we note that the conceptual framework presented in Figure 1 can be adapted to diagnose concurrent and lagged ecosystem state changes on any timescale of relevance.

2.2 Model and drivers

We use the data-assimilation linked ecosystem carbon model (DALEC; Williams et al., 2005) to represent the principal terms and major pathways of the terrestrial C cycle. The DALEC model family has been extensively used to diagnose terrestrial C cycle dynamics across a range of site level and spatially resolved approaches (Fox et al., 2009; Rowland et al., 2014; Bloom et al., 2016; Smallman et al., 2017; Exbrayat et al., 2018; amongst several others). Here we use DALEC version 2a (henceforth DALEC2a): a summary of the DALEC2a states and processes is depicted in Figure 2. For the sake of brevity, we solely report changes in reference to DALEC2 (previously described by Bloom et al., 2016), and refer the reader to the supplementary material (and references therein) for a complete description of the model.

We extended the DALEC2 structure to include first-order plant-available water (H_2O) pool, where the hydrological balance is defined as the sum of precipitation inputs (P) and evapotranspiration (ET) and runoff (R) outputs. In turn, the plant-available H_2O limits gross primary productivity, through conservation of the inherent water-use efficiency (Beer et al., 2009), where ET is calculated as a function of gross primary production (GPP) and atmospheric vapor pressure deficit (Appendix B1). Effectively, the interaction between plant-available H_2O, GPP and ET constitutes a first-order plant-soil carbon-water feedback. We further appended the DALEC2 structure by including a parameterization of soil moisture limitation on

heterotrophic respiration (Appendix B2), given that heterotrophic respiration dependence on soil moisture remains highly uncertain (Moyano et al., 2013; Sierra et al., 2015), as well as a dominant source of uncertainty amongst terrestrial C models (Falloon et al., 2011; Exbrayat et al., 2013a,b).

Given a range of in-situ and continental-scale studies highlighting the uncertainties of fire combustion factors across a range of ecosystems, (Ward et al., 1996; Bloom et al., 2015), the errors involved in representing fine-scale fire type variability (Giglio et al., 2013), and spatial variability of fuel loads, we optimize fire C pool combustion factors (in contrast, combustion factors were prescribed as constants in Bloom et al., 2016): specifically, we optimize the combustion factors of foliar biomass (π_{foliar}), non-foliar biomass pools (π_{nfb}), soil C (π_{SOM}) and the fire resilience factor (we approximate the litter C combustion factor as the arithmetic mean of π_{foliar} and π_{SOM}, given that the DALEC2a litter pool represents both above-ground and below-ground C reservoirs). Prior ranges for all π and the fire resilience are conservatively defined as spanning 0.01 to 1. We implement the ecological and dynamic constraints (Bloom & Williams 2015) to ensure that foliar C combustion factors are greater than both non-foliar biomass and soil C combustion factors ($\pi_{foliar} > \pi_{nfb}$ and $\pi_{foliar} > \pi_{SOM}$) which are comprehensively consistent with detailed measurements of C pool combustion factors across a range of ecosystem fire types (Shea et al., 1996; Araújo et al., 1999, van Leeuwen et al., 2014 amongst others). Finally, we also represent the uncertainty in the longevity of plant labile C; specifically, we now optimize—rather than prescribe—the labile C lifespan used during leaf flushing in DALEC2a (previously all labile C was used during leaf flush, see Bloom & Williams, 2015). The updated model structure is depicted in Figure 2. We henceforth summarize the dynamical description of DALEC2a as

$$\boldsymbol{x}_{t+1} = DALEC2a(\boldsymbol{x}_t, \boldsymbol{M}_t, \boldsymbol{p}) \quad (1),$$

where $\boldsymbol{x}_t$ represents the ecosystem state vector at time t, $\mathbf{M}_t$ represents the corresponding meteorological and disturbance forcings (namely monthly temperature, precipitation, global radiation, vapor pressure deficit, burned area and atmospheric CO_2), $\boldsymbol{p}$ represents a vector of time-invariant process parameters and $DALEC2a()$ represents the DALEC2a operation on states x_t throughout time $t \rightarrow t+1$. In summary, DALEC2a optimizable quantities consist of 26 process parameters, $\boldsymbol{p}$, and seven initial ecosystem states (C and H_2O pools; Figure 2) at timestep t=0, $\boldsymbol{x}_0$. For the sake of brevity, we include a complete description of DALEC2a state variables, process parameters and diagnostic C fluxes in the supplementary material, except where an explicit mention is necessary in the manuscript.

2.3 Observations

The observations assimilated into CARDAMOM are summarized in Table 1. Following Bloom et al., (2016) we assimilate Moderate Imaging Spectroradiometer (MODIS) leaf area index (LAI), soil organic matter (SOM) from the Harmonized world soil database (HWSD; Hiederer & Köchy, 2011) and above- and below-ground biomass (ABGB, Saatchi et al., 2011). Solar-

induced fluorescence (SIF)—retrieved from the Greenhouse Gases Observing Satellite (GOSAT)—is a robust proxy for photosynthetic activity: while non-linear inter-relationships at plant level and flux-tower level have been observed under certain conditions (Verma et al., 2017, Magney et al., 2017), GPP is observed to be linearly inter-related with SIF at ecosystem and regional scales (Frankenberg et al., 2011; Sun et al., 2017). Given that SIF:GPP linear relationships are known to vary substantially across individual species and entire ecosystems, here we solely assume that monthly SIF provides a constraint on the relative temporal variability of GPP (following MacBean et al., 2018). The monthly averaged 2010-2015 4°×5° SIF values were derived with the polarizations and selection criteria described by Parazoo et al., (2014). The assimilation of relative SIF variability is described in section 2.4.

We assimilate the GOSAT-derived 2010-2013 net biospheric C exchange (NBE) dataset (NBE > 0 for a net biosphere-to-atmosphere flux) estimated using the Carbon Monitoring System Flux atmospheric CO_2 inversion framework (CMS-Flux; Liu et al., 2014, 2018). In summary, total monthly 4°×5° surface CO_2 fluxes were scaled using a Bayesian 4D variational (4D-Var) inversion approach in order to minimize differences between GOSAT 2010-2013 observations and CMS-Flux representations of total column CO_2 (we refer the reader to Liu et al., 2018 for additional details on the derivation of surface CO_2 fluxes). Following Liu et al., (2017) and Bowman et al. (2017), we subtract prior estimates of anthropogenic CO_2 emissions from total CMS-Flux total CO_2 flux estimates, and we assume that prior anthropogenic CO_2 emissions errors are minimal compared to the biospheric CO_2 fluxes, given that these are typically much smaller than natural CO_2 fluxes at a 4°×5° resolution across the tropics. We withhold 2015 CMS-Flux NBE estimates—constrained by Orbiting Carbon Observatory (OCO-2) total column CO_2 observations (Liu et al., 2017)—to validate CARDAMOM 2015 regional NBE estimates and their associated uncertainties in the absence of CO_2 constraints (OCO-2 NBE estimates are therefore withheld from the CARDAMOM NBE assimilation step described in section 2.4); in effect, we employ the validation of CARDAMOM NBE predictions against withheld data effect as a means for evaluating the mechanistic representations of CARDAMOM's time-varying C cycle processes.

Finally, we assimilate mean 2001-2015 fire C emission estimates derived from monthly 4°×5° satellite-based estimates of fire CO emissions (Jiang et al., 2017; Worden et al., 2017; Bloom et al., 2019): the estimates of biomass burning CO emissions were derived based on an ensemble of atmospheric CO inversions of column CO measurements from the Measurements of Pollution in the Troposphere (MOPITT) instrument onboard the NASA EOS/TERRA satellite (Deeter et al., 2014). We refer the reader to Jiang et al., (2017) for the details of the atmospheric CO inversion using the GEOS-Chem adjoint model and to Worden et al., (2017) for the attribution of optimized CO fluxes to biomass burning. Biomass burning CO emission estimates by Worden et al., (2017) were then used to derive total biomass burning C emissions based on monthly estimates of CO_2:CO; the approach is detailed in Bowman et al., (2017). We note that NBE estimates exhibit substantial spatial error covariance structures across individual 4°×5° grid-cells, and the effective information content of the NBE inversions is larger than the 4°×5° resolution. To mitigate the spatial error correlation features identified in the NBE dataset (Bowman et al., 2017; Liu et

al., 2017), we employed a 3×3 gridcell smoothing window for monthly NBE estimates, following the approach by Liu et al. (2018).

2.4 Model-data fusion

Within each 4°×5° grid cell, the C cycle dynamics in DALEC are a function of meteorological and disturbance drivers $\boldsymbol{M}$, model parameters $\boldsymbol{p}$ and initial conditions $\boldsymbol{x}_0$ (as summarized in Eq. 1). We use a Bayesian inference formulation to independently retrieve the optimal distribution of $\boldsymbol{x}_0$ and $\boldsymbol{p}$ given observations $\boldsymbol{O}$ for each 4°×5° grid cell, where:

$$p(\boldsymbol{y}|\boldsymbol{O}) \propto p(\boldsymbol{y})p(\boldsymbol{O}|\boldsymbol{y}) \quad (2);$$

$\boldsymbol{y}$ is the control vector $\{\boldsymbol{x}_0,\boldsymbol{p}\}$, p($\mathbf{y}$) is the prior probability distribution of $\boldsymbol{y}$, and p($\boldsymbol{O}|\boldsymbol{y}$) is proportional to the likelihood of $\boldsymbol{y}$ given $\boldsymbol{O}$, $L(\boldsymbol{y}|\boldsymbol{O})$. At any given grid cell, the observation vector $\boldsymbol{O}$ consists of LAI, SOM, ABGB, SIF, NBE and CO-derived fire CO_2 emissions (henceforth $\boldsymbol{O}_{LAI}$, $\boldsymbol{O}_{SOM}$, $\boldsymbol{O}_{ABGB}$, $\boldsymbol{O}_{SIF}$, $\boldsymbol{O}_{NBE}$ *and* $\boldsymbol{O}_{CO}$ respectively), and—assuming errors are uncorrelated—the overall likelihood of $\boldsymbol{y}$ given $\boldsymbol{O}$ can be expressed as

$$L(\boldsymbol{y}|\boldsymbol{O}) = L_{LAI}\, L_{SOM}\, L_{ABGB}\, L_{SIF}\, L_{NBE}\, L_{CO} \quad (3)$$

For LAI, SOM, ABGB and CO, we derive the corresponding likelihood function L_* (i.e. L_{LAI}, L_{SOM}, L_{ABGB} and L_{CO}, respectively) as follows:

$$L_* = \mathrm{e}^{-\frac{1}{2}\sum_i\left(\frac{m_i(y)-o_i}{\sigma_i}\right)^2} \quad (4)$$

where o_i and $m_i(\boldsymbol{y})$ correspond to the ith observation and corresponding modeled quantity derived from control vector $\boldsymbol{y}$, respectively; σ_i represents the combined errors of model and data, namely the combined effects of DALEC model structural error, model driver errors and observation errors. In contrast to Bloom et al., 2016, given that MODIS LAI retrievals have exhibited systematic seasonal biases across the wet tropics (Bi et al., 2015), we solely use mean LAI as a constraint on the mean DALEC2a LAI values (therefore, for the derivation of L_{LAI}, m and o in equation 3 correspond to the 2001-2015 mean modeled and observed LAI).

To constrain the relative variability of GPP based on SIF without imposing constraints on the absolute GPP magnitude, we derive L_{SIF}—based on Eq.4—by formulating m and o as follows:

$$m_i(\boldsymbol{y}) = \frac{GPP_i}{\overline{\boldsymbol{GPP}}} \quad (5),$$

$$o_i = \frac{SIF_i}{\overline{\boldsymbol{SIF}}} \quad (6),$$

where SIF_i and GPP_i are SIF and corresponding DALEC2a GPP values at time index i and $\overline{\boldsymbol{SIF}}$ and $\overline{\boldsymbol{GPP}}$ are the corresponding means during the 2010-2015 time period.

We constrain CARDAMOM NBE using 4°×5° monthly CMS-Flux NBE estimates, derived from GOSAT atmospheric total column CO_2 retrievals (Liu et al., 2018) spanning 2010-2013. At each 4°×5° location, we define the L_{NBE} as the product of mean annual NBE and seasonal NBE anomalies using the following equation:

$$L_{NBE} = \mathrm{e}^{-\frac{1}{2}\sum_a\left(\frac{\mathrm{m}'_a(y)-o'_a}{\sigma'}\right)^2} \mathrm{e}^{-\frac{1}{2}\sum_{i,a}\left(\frac{m''_{i,a}(y)-o''_{i,a}}{\sigma''}\right)^2} \quad (7),$$

where m'_a denotes annual mean DALEC2a NBE value for year a and $m''_{i,a}$ denote DALEC2a NBE seasonal deviations from their annual means; specifically, for a given month i with corresponding year a:

$$m'_a(\boldsymbol{y}) = \frac{1}{12}\sum_{i=1}^{12} NBE_{i,a} \quad (8)$$

$$m''_{i,a}(\boldsymbol{y}) = NBE_{i,a} - m'_a \quad (9)$$

where $NBE_{i,a}$ is the DALEC2a NBE; observations o'_a and $o''_{i,a}$ were derived identically to m'_a and $m''_{i,a}$. Similarly to Desai (2010), we implement the likelihood function outlined in Eq. 7 in order to capture both the seasonal and inter-annual modes of NBE variability; we found that solely minimizing the monthly NBE residuals following the formulation based on Eq. 4 led to disparate inter-annual variations between the model and observation-constrained NBE. Effectively the formulation in Eq. 7—in comparison to Eq. 4— increases the relative weight of mean annual CMS-Flux NBE constraints on DALEC2a NBE.

The uncertainty for each observational constraint (i.e. σ values in Eq. 4 and 7) implicitly represent the combined impacts of observational random errors, systematic errors, and model structural error. In the absence of knowledge on the relative roles of observation errors in the monthly 4°×5° observation uncertainties and explicit knowledge of model structural error, we prescribed σ values through trial and error, in order to (a) ensure that model states and diagnostic variables capture the predominant variability of the observational constraints **O**, while (b) ensuring that σ values are comparable to the observational uncertainty. For all land surface variables (namely LAI, ABGB, SOM and SIF), m and o were log-transformed (following Bloom et al., 2016). For the mean 2001-2015 LAI constraint, we assumed log-normal uncertainty of σ=±log(1.2); we prescribed σ = ±log(2) log-normal uncertainty structure for each SIF observation. We approximated the uncertainty of the CO-

derived mean 2001-2015 fire C values as σ = ± 20%, which is broadly consistent with the monthly 4°×5° CO uncertainty estimates and the corresponding CO_2:CO uncertainty estimates reported by Bowman et al., (2017) and Worden et al., (2017). For NBE we prescribed σ'= 0.02 gC/m2/day and σ''= 2 gC/m2/day; we found that these were suitable to capture the first-order 2010-2013 seasonal and inter-annual components of continental scale NBE variability. The uncertainties assumed for each observational constraint are summarized in Table 1; we note that these implicitly include the combined assumption on observational random errors, systematic errors, and model structural error. We discuss the potential impacts of observation uncertainty assumptions and make recommendation for future efforts in section 3.3.

To retrieve the distribution of p($\boldsymbol{y}|\boldsymbol{O}$), we employed an adaptive metropolis-Hastings Markov Chain Monte Carlo (MHMCMC) approach following Bloom et al., (2016) to sample the objective function, namely the product of p(y) and p(O|y); for reference, we list the individual components of the objective function in the manuscript supplement (section S3). We generally found that the computational costs required to meet MHMCMC convergence criterion reported by Bloom & Williams (2015) for each 4°×5° grid-cell were prohibitively expensive. We updated the adaptive MHMCMC to the Haario et al., (2001) MHMCMC approach, where the MHMCMC proposal distribution is adapted as a function of previously accepted samples (see Haario et al., 2001 for algorithm details). We ran 4 adaptive MHMCMC chains for 10^8 iterations in each 4°×5° grid-cell. We found that the latter half of the chains converged within a Gelman-Rubin convergence criterion value of <1.2 in 75% of the grid cells. For the subsequent analysis, we use a subset of 500 samples of $\boldsymbol{y}$ from the of latter half of each MHMCMC chain, totaling 4×500 samples of $\boldsymbol{y}$ per 4°×5° grid-cell.

2.5 Dynamical formulation of concurrent and lagged effects

Here we present a dynamical formulation for the derivation of concurrent and lagged effects on the inter-annual ecosystem state changes. To explicitly quantify the concurrent effects and lagged effects, we define the trajectory of the modeled dynamic state variables $\boldsymbol{x}$ at year $a+1$ as

$$\boldsymbol{x}_{a+1} = D(\boldsymbol{x}_a, \boldsymbol{M}_a, \boldsymbol{p}) \quad (10),$$

where the state vector $\boldsymbol{x}_{a+1}$—which is comprised of DALEC2a states at the beginning of year a+1—is computed from the DALEC2a model operator D(), which is a function of the previous state $\boldsymbol{x}_a$ at beginning of year a, the meteorological and disturbance forcing history of the previous year $\boldsymbol{M}_a$, and time-invariant ecosystem parameters $\boldsymbol{p}$. We note that Eq. 10 is resolved on an annual time-step; however, the DALEC2a operator time-step is monthly, hence the operator in Eq. 10 is a composite of monthly operators as denoted in equation 1. To isolate the role of concurrent meteorological and disturbance anomalies in $\boldsymbol{M}_a$, we define the C trajectory under a reference climatological mean forcing $\boldsymbol{M}'$ as

$$\boldsymbol{x'}_{a+1} = D(\boldsymbol{x}_a, \boldsymbol{M'}, \boldsymbol{p}) \quad (11).$$

Here we define $\boldsymbol{M'}$ as the monthly climatological mean of the 2001-2015 meteorological and disturbance drivers and $\boldsymbol{\delta M_a}$ as the corresponding anomaly in year *a*, where

$$\boldsymbol{M}_a = \boldsymbol{M'} + \boldsymbol{\delta M_a}. \quad (12).$$

With Eq. 10 and 11, we can define the change in the state $\boldsymbol{x}$ in year *a*, $\delta \boldsymbol{x}_a$, as

$$\delta \boldsymbol{x}_a = \boldsymbol{x}_{a+1} - \boldsymbol{x}_a = (\boldsymbol{x}_{a+1} - \boldsymbol{x'}_{a+1}) + (\boldsymbol{x'}_{a+1} - \boldsymbol{x}_a) \quad (13).$$

This formulation allows us to define the lagged effect on ecosystem states in year *a* as

$$\delta \boldsymbol{x}_a^{LAG} = \boldsymbol{x'}_{a+1} - \boldsymbol{x}_a \quad (14),$$

and the concurrent effect on ecosystem states in year *a* as

$$\delta \boldsymbol{x}_a^{CON} = \boldsymbol{x}_{a+1} - \boldsymbol{x'}_{a+1} \quad (15);$$

and the sum of concurrent and lagged effects in Eq. 14 and 15 as

$$\delta \boldsymbol{x}_a = \delta \boldsymbol{x}_a^{LAG} + \delta \boldsymbol{x}_a^{CON} \quad (16).$$

We conceptually illustrate the derivation of annual concurrent and lagged effects on a given ecosystem state *x* in Figure 3. Under a climatological mean forcing (blue line), the ecosystem state trajectory—solely induced by lagged processes—would diverge from externally forced ecosystem state trajectory (black line), and would eventually converge to an equilibrium state or oscillate about a domain of attraction (Figure 3a). For a one-year timespan, the change in ecosystem state *x* throughout year *a*, $\delta \boldsymbol{x}_a$ can be decomposed into a climatology-induced lagged effect change $\delta \boldsymbol{x}_a^{LAG}$, and an anomaly-induced concurrent effect change $\delta \boldsymbol{x}_a^{CON}$ (Figure 3a, inset).

From a mechanistic standpoint, the variability of $\delta \boldsymbol{x}_a^{LAG}$ is independent of meteorological forcing anomalies and is therefore solely dependent on all ecosystem states $\boldsymbol{x}_a$. For example, in a hypothetical scenario where a climatological mean forcing induces no net ecosystem state changes, then $\delta \boldsymbol{x}_a^{LAG} = \boldsymbol{x_a} - \boldsymbol{x'}_{\boldsymbol{a+1}} = \boldsymbol{0}$, and $\delta \boldsymbol{x} = \delta \boldsymbol{x}^{CON}$. In a more general scenario,

$\delta \boldsymbol{x}_a^{LAG} = \boldsymbol{x_a} - \boldsymbol{x'}_{a+1} \sim constant$ for all a: in this instance $\boldsymbol{x}_a^{LAG}$ is non-zero but largely insensitive to variations in $\boldsymbol{x}_a$ within a typical range of ecosystem states $\boldsymbol{x}$, therefore (i) the year-to-year variability of $\delta \boldsymbol{x}$, is largely dependent on the variability of $\delta \boldsymbol{x}^{CON}$, and (ii) $\delta \boldsymbol{x}^{LAG}$ amounts to an approximately constant offset term (Figure 3b). Alternatively, if $\delta \boldsymbol{x}^{LAG}$ is sufficiently sensitive to the variability of $\boldsymbol{x}$, the variability of $\delta \boldsymbol{x}$ will be a function of both $\delta \boldsymbol{x}^{LAG}$ and $\delta \boldsymbol{x}^{CON}$: in this instance, year-to-year variations in $\boldsymbol{x}$ are influencing both the sign and magnitude of lagged effects (Figure 3c).

Here we investigate the possible contributions of the annual variability of $\delta \boldsymbol{x}^{CON}$ and $\delta \boldsymbol{x}^{LAG}$ on $\delta \boldsymbol{x}$ for the 2001-2015 time period across tropical ecosystems. Specifically, we test the two following hypotheses:

- *Hypothesis 1*: $var(\delta \boldsymbol{x}^{LAG}) \ll var(\delta \boldsymbol{x}^{CON})$. In this instance, the impact of $\boldsymbol{M'}$ on $\boldsymbol{x}$ is largely independent on the variability of $\boldsymbol{x}$; consequently the year-to-year variability of the lagged effects force $\delta \boldsymbol{x}^{LAG}$ is relatively small, and the year-to-year changes in ecosystem states, $\delta \boldsymbol{x}$, are dominated by $\delta \boldsymbol{x}^{CON}$ (Figure 3b).
- *Hypothesis 2*: $var(\delta \boldsymbol{x}^{LAG}) \sim var(\delta \boldsymbol{x}^{CON})$. In this instance, the impact of $\boldsymbol{M'}$ on $\boldsymbol{x}$ is dependent on the variability of $\boldsymbol{x}$; consequently, the year-to-year variability of the lagged effects $\delta \boldsymbol{x}^{LAG}$ is substantial, and the year-to-year changes in ecosystem states, $\delta \boldsymbol{x}$, are substantially attributable to both $\delta \boldsymbol{x}^{CON}$ and $\delta \boldsymbol{x}^{LAG}$ (Figure 3c).

The mechanistic nature of the DALEC2a model within CARDAMOM (namely the representation of allocation fractions, residence times, meteorological sensitivities and explicit representation of dynamical states) allows for a data-constrained probabilistic assessment of the relative role lagged and concurrent effects on net ecosystem state changes. The disaggregation of $\delta \boldsymbol{x}_a$ into $\delta \boldsymbol{x}_a^{CON}$ and $\delta \boldsymbol{x}_a^{LAG}$ (and the associated hypotheses 1 and 2) can be projected onto any subset of net ecosystem fluxes or additive combination of gross fluxes. For example, the NBE in year a (NBE_a) corresponds to the net C loss between $\boldsymbol{x_a}$ and $\boldsymbol{x_{a+1}}$; in turn, NBE_a can be decomposed into its lagged effect component (NBE_a^{LAG}) and the concurrent effect component (NBE_a^{CON}), where

$$NBE_a = NBE_a^{CON} + NBE_a^{LAG} \quad (17);$$

NBE_a and NBE_a^{LAG} can be directly calculated from $D(\boldsymbol{x}_a, \boldsymbol{M}_a, \boldsymbol{p})$ and $D(\boldsymbol{x}_a, \boldsymbol{M'}, \boldsymbol{p})$ respectively, and NBE_a^{CON} is calculated as $NBE_a - NBE_a^{LAG}$. By definition in the DALEC2a model, NBE is the sum of primary productivity (NPP), heterotrophic respiration (RHE) and fire (FIR) fluxes, where:

$$NBE_a = RHE_a + FIR_a - NPP_a \quad (18).$$

In turn, disaggregation *RHE*, *FIR* and *NPP* into their respective concurrent and lagged components gives:

$$NBE_a^{CON} = RHE_a^{CON} + FIR_a^{CON} - NPP_a^{CON} \quad (19).$$

$$NBE_a^{LAG} = RHE_a^{LAG} + FIR_a^{LAG} - NPP_a^{LAG} \quad (20).$$

To diagnose relative inter-annual variations of a given flux $\boldsymbol{F}$ (namely the 2001-2015 timeseries of *NBE*, *RHE*, *FIR* and *NPP*), we derive annual anomalies $\Delta\boldsymbol{F}$ relative to the mean 2001-2015 flux $\overline{\boldsymbol{F}}$, where for a given year a:

$$\Delta F_a = F_a - \overline{\boldsymbol{F}} \quad (21).$$

The Δ operation in Eq. 21 can be implemented onto each term in Eq. 18-20 without loss of equivalence between left-hand and right-hand sides (for example, $\Delta NBE_a^{LAG} = \Delta RHE_a^{LAG} + \Delta FIR_a^{LAG} - \Delta NPP_a^{LAG}$).

Finally, we diagnose the 2001-2015 ΔNBE_a^{LAG} variability as a function of the inter-annual anomalies in individual ecosystem states, $\Delta\boldsymbol{x}_{a(*)} = \{\Delta x_{a(1)}, \Delta x_{a(2)}, \ldots, \Delta x_{a(N)}\}$, relative to the mean ecosystem state $\overline{\boldsymbol{x}}$. For DALEC2, these consist of annual anomalies in initial C and H_2O states (see Figure 2). For a given year, the total NBE lagged effect anomaly, ΔNBE_a^{LAG} can be decomposed into

$$\Delta NBE_a^{LAG} = \sum_{n=1}^{N} \Delta NBE_{a(n)}^{LAG} + \Delta I_a \quad (22);$$

$\Delta NBE_{a(n)}^{LAG}$ represents the NBE lagged effect component solely attributable to an anomaly in ecosystem state n ($\Delta x_{a(n)}$), and ΔI_a collectively accounts for the contribution of higher-order interactions between individual ecosystem states. In other words, given that ΔNBE_a^{LAG} is solely attributable to variability of annual initial conditions $\boldsymbol{x}_a$, the decomposition of ΔNBE_a^{LAG} to individual pool contributions provides a first-order attribution of lagged effect IAV to underlying C and H_2O pool dynamics. The derivation of Eq. 22 is explicitly described in Appendix C.

To derive uncertainty estimates for each annual flux F_a, or corresponding anomaly ΔF_a, we calculate each term based on the 2000 samples of $\boldsymbol{y}$ at each gridcell (see section 2.4), and we calculate the corresponding median and inter-quartile range (25^{th}-75^{th} percentiles) for each term. Inter-annual variations in 2001-2015 $\boldsymbol{F}$ and $\Delta\boldsymbol{F}$ timeseries are reported as standard deviations of median values. We conservatively assume that $\boldsymbol{F}$ and $\Delta\boldsymbol{F}$ errors are fully correlated when propagating these uncertainties across each region.

3. Results and Discussion

3.1. Evaluation of observation-constrained tropical C balance

Ultimately inferences about the concurrent and lagged effects on NBE can only be drawn if the CARDAMOM analysis is able to both (i) accurately represent observed NBE, and (ii) accurately represent underlying states and processes controlling IAV. To assess the CARDAMOM 2001-2015 re-analysis, here we present an evaluation of CARDAMOM against (a) the assimilated 2010-2013 GOSAT-derived NBE dataset, and (b) the withheld OCO-2 derived 2015 NBE dataset, and (c) assimilated and independent datasets of tropical terrestrial ecosystem states and fluxes.

Optimized CARDAMOM NBE (a function of the optimized DALEC2a parameters and initial 2001 ecosystem states) broadly represents the monthly variability of the 2010-2013 regional-scale assimilated GOSAT-retrieved NBE (Figure 4; Table 2). In individual regions, monthly CARDAMOM versus CMS-Flux NBE r $\geq$ 0.69, with the exception of South-East Asia and Indonesia region (r = 0.57) where the CARDAMOM and GOSAT-retrieved NBE exhibits a relatively small seasonality compared to other regions. Evaluation of CARDAMOM NBE against withheld NBE estimates from OCO-2 exhibit a degradation in the correlation and RMSE values, but agree favorably on the amplitude and timing of the NBE variability (Table 2). We find that the CARDAMOM analysis is able to robustly capture the 2010-2013 GOSAT-derived NBE IAV at regional scales (see Figure 5 & Table 2; regional NBE r $\geq$ 0.9). On an annual basis, all regional OCO-2 annual NBE estimates 2015 except northern hemisphere South America are within the 90% CARDAMOM prediction confidence intervals (Figure 5); furthermore, all OCO-2 annual NBE estimates are within CARDAMOM 2015 prediction confidence intervals for the wet tropics, dry tropics and the entire tropical study region. We also note that regions the confidence intervals outside the 2010-2013 period predictions exhibit substantially larger than uncertainty, mainly due to under-constrained modes of long-term terrestrial C cycle variability. We found generally lower seasonal correlations between CARDAMOM NBE and GOSAT-retrieved across 4°×5° gridcells (Figure S2; 25^{th} – 75^{th} percentile = 0.19 - 0.63), and corresponding annual mean correlations (25^{th} – 75^{th} percentile = 0.31 - 0.89) relative to the sub-continental and pantropical regions (Table 2); the lower correlative agreement is likely due to the limited 4°×5° information content of satellite-based NBE flux estimates (Liu et al., 2014, Bowman et al., 2017).

We also evaluate the 2001-2015 CARDAMOM NBE against the inter-annual variability of the NOAA ESRL surface-based global atmospheric CO_2 growth rate observations (www.esrl.noaa.gov/gmd/ccgg/trends/; see supplementary information for dataset details). We assume that the atmospheric CO_2 growth rate variability—once detrended to remove decadal trends in fossil fuel emissions and ocean CO_2 uptake and biogenic CO_2 uptake—predominantly exhibit inter-annual variations of the tropical C balance (Baker et al., 2006; Cox et al., 2013; Sellers et al., 2018). We find that 2001-2015 detrended CARDAMOM NBE (Figure 5, bottom-right panel), exhibits broad consistency with atmospheric CO_2 growth rate; the detrended datasets exhibit comparable levels of inter-annual variability (atmospheric CO_2 growth rate IAV = ± 0.62 PgC/yr, CARDAMOM

tropical NBE IAV = ± 0.80 PgC/yr) as well as a significant correlations between annual NBE growth rate anomalies (r = 0.62, pval=0.01).

The spatial variability of CARDAMOM state variables and fluxes constrained by static datasets, namely LAI, biomass, soil C and mean fire C emissions (Table 1), are broadly correlated with the observational constraints by the CARDAMOM analysis (r = 0.7 – 0.98; p<0.05; Figure S2); for the above-mentioned quantities total median errors amounted to <10%, with the exception of soil C (median error CARDAMOM soil C = 25%). The correlation between CARDAMOM GPP and GOSAT SIF is positive & significant (p-value <0.05) in 67% of 4°×5° pixels, with higher correlations in the dry tropics (25^{th} – 75^{th} percentile = 0.41 – 0.78) relative to the wet tropics (25^{th} – 75^{th} percentile = 0.13 – 0.63); the lower correlations in the wet tropics are generally expected, given that wet tropical ecosystems fundamentally exhibit a weaker GPP seasonal cycle.

We also evaluate the mean and inter-annual variability of CARDAMOM GPP, ET and LAI outputs against (i) two independent measurement-based GPP estimates for 2007-2015 (FLUXCOM GPP, Jung et al., 2020; and FLUXSAT GPP, Joiner et al., 2018), (ii) two independent measurement-based ET estimates (FLUXCOM ET, Jung et al., 2019; MODIS ET, Mu et al., 2011) for 2001-2013, and (iii) 2001-2015 MODIS LAI (we note that only mean 2001-2015 MODIS LAI was assimilated into CARDAMOM; see section 2.3). Datasets details and regional evaluations are included section S2 and Tables S2-S3 in the supplementary material. In summary, we find that mean CARDAMOM pantropical GPP is within 20% of both independent estimates and regional estimates are within 40% of both independent estimates; regional GPP IAV in CARDAMOM (0.8 – 7.4%) is broadly consistent with FLUXSAT GPP (1.3-10.7%) and FLUXCOM GPP (0.3 – 4.2%). Pan-tropical GPP correlations are positive and significant (p-value < 0.05) among all three estimates (r = 0.69 – 0.74); regional correlations are by and large positive but not significant. CARDAMOM mean ET values are lower but withing 25% of independent ET estimates, and differences in regional mean ET are within 50% of independent estimates; regional ET IAV in CARDAMOM (2.3 % - 5.5%) is broadly consistent with FLUXCOM ET (0.3 – 5.9%) and MODIS ET (1.3 – 13.4%). Correlations between three datasets span positive and negative values but are mostly not significant; regional CARDAMOM ET correlations against MODIS and FLUXCOM (r = -0.64 – 0.41) are generally lower than inter-agreement between the two datasets (r = -0.27 – 0.94). Mean CARDAMOM LAI is within 15% of MODIS LAI across all regions. Regional CARDAMOM LAI values (1.6 - 4.8%) are broadly consistent with the range of MODIS LAI values (0.7 – 5.2%); none of the regional correlation values were significant. The notable lack of correlative agreement between CARDAMOM and independent LAI and ET estimates is potentially due to (a) the lack of direct observational constraints on the temporal variability of ET and LAI in CARDAMOM, and/or (b) systematic errors or limitations of independent LAI and ET estimation approaches on inter-annual timescales (Bi et al., 2015; Pan et al., 2020), and/or (c) fundamental limitations of CARDAMOM ET and LAI estimates (further discussed in section 3.3).

Overall, we argue that (i) CARDAMOM NBE and associated uncertainties compare favorably against withheld and independent data on seasonal and inter-annual timescales, and (ii) the spatial variability and the IAV magnitude of CARDAMOM ancillary states and fluxes are in general agreement with a range of assimilated and independently estimated quantities. We discuss noteworthy caveats and limitations of retrieved CARDAMOM ecosystem dynamics—and the implications on inferred variability of concurrent and lagged effects—in section 3.3. We anticipate that the ever-growing satellite CO_2 record, along with increasing volume and quality of terrestrial ecosystem observations, will ultimately lead to improved seasonal and inter-annual process representations in future model-data fusion analyses of the terrestrial C balance.

3.2 Concurrent and lagged effects on the tropical C balance

The attribution of annual ΔNBE into its concurrent and lagged components (ΔNBE^{CON} and ΔNBE^{LAG}) reveals that both are prominent contributors to regional and pan-tropical ΔNBE (Figure 6). On a regional scale, ΔNBE^{CON} IAV and ΔNBE^{LAG} IAV during 2001-2015 amount to 61-107% and 41-122%, respectively, relative to ΔNBE IAV (Table 3). Notable ΔNBE^{CON} anomalies include (i) the positive ΔNBE^{CON} values in both South America regions during drier conditions in 2005, 2007 and 2010, in contrast negative ΔNBE^{CON} responses during wetter conditions in 2009 and 2011, and (ii) negative ΔNBE^{CON} values during the relatively wet 2010-2011 conditions in Australia; both continental-scale responses corroborate the generally hypothesized responses of tropical ecosystems to wet and dry extreme events (Lewis et al., 2011; Bastos et al., 2013). For the most part, both ΔNBE^{CON} and ΔNBE^{LAG} contribute substantially to the year-to-year ΔNBE anomaly changes on a regional scale. Across the wet tropics, the sign of the largest ΔNBE anomalies are predominantly explained by ΔNBE^{CON}; in contrast, dry tropics ΔNBE^{LAG} IAV and ΔNBE^{CON} IAV both substantially contribute to annual ΔNBE anomalies. Instances where ΔNBE^{LAG} or ΔNBE^{CON} IAV values amount to >100% of ΔNBE IAV are attributable to regional and pan-tropical anti-correlations between ΔNBE^{LAG} and ΔNBE^{CON}: specifically, ΔNBE^{LAG} and ΔNBE^{CON} are anticorrelated across the tropics (r = -0.05), and all regions except SE Asia & Indonesia (r = -0.56–0.14); the consistent anticorrelation across five out of six regions suggests that lagged effects may significantly and systematically dampen the impact of ΔNBE^{CON}. On a pan-tropical scale, we found that ΔNBE^{CON} IAV and ΔNBE^{LAG} IAV are both substantial contributors to NBE IAV (80% and 64%); the relative importance of ΔNBE^{LAG} IAV relative to ΔNBE^{CON} is largest in the dry tropics (83% and 99%, respectively), and remains substantial albeit smaller in wet tropics (79% and 45%, respectively). Uncertainties in ΔNBE, ΔNBE^{CON} and ΔNBE^{LAG} (Figure 6) are generally linked to confounding NBE trend uncertainties throughout 2001-2015 (Figure 4), particularly on a pantropical scale where NBE uncertainties are considerably larger than median NBE IAV. To directly assess the uncertainty of ΔNBE^{LAG} IAV contributions to NBE IAV irrespective of annual NBE uncertainties, we (a) rank all 4°×5° grid-cell CARDAMOM samples by their corresponding 2001-2015 ΔNBE^{LAG} IAV, and (b) combine CARDAMOM samples by ranking to generate a corresponding ensemble of regional and pan-tropical ΔNBE^{LAG} IAV estimates (summarized in Table S5). We find that the regional 95% confidence ranges are all within 50% of the median ΔNBE^{LAG} IAV values reported in Table 3. Notably, the ensemble of pan-tropical ΔNBE^{LAG} IAV estimates span 42% - 97% of NBE IAV (2.5^{th} – 97.5^{th} percentile range), indicating that—even under

overwhelmingly conservative assumptions on grid-cell ΔNBE^{LAG} IAV—lagged effects are invariably a prominent component of tropical NBE IAV.

Variations in ΔNBE^{LAG} throughout 2001-2015 include a range of lagged processes spanning between (a) ΔNBE^{LAG} changes induced by recent forcing events (b) the gradual changes in ΔNBE^{LAG} attributable to an ecosystem's approach or oscillation around a domain of attraction (see section 2.1). Notably, even in the absence of a recent forcing event, ΔNBE^{LAG} will potentially continue to change in magnitude from year to year as ecosystem states approach or oscillate around a domain of attraction. We conducted a sensitivity test for southern hemisphere South America region (top-left panel of Figure 6) to disentangle the range of contributions to 2001-2015 ΔNBE^{LAG} values: specifically, we (a) resolve ΔNBE^{LAG} in the absence of 2001-2015 forcing anomalies, and (b) sequentially add 2001-2015 forcing anomalies to resolve ΔNBE^{LAG} attributable to annual forcing events (Figure S6). In the absence of 2001-2015 forcing anomalies, lagged effects account for a ±0.11 PgC/yr variability in total NBE, explained by an approximately linear +0.02 PgC/yr increase throughout the 2001-2015 time period. The sequential addition of 2001-2015 forcing anomalies indicates the sign and magnitude of lagged effects are substantially influenced by annual forcing events; while the inter-annual variability modestly increased to ±0.13 PgC/yr, year-to-year changes exceed 0.3 PgC/yr (Figure 6). Furthermore, while most years induced relatively short-lived (1-2 years) contributions to subsequent ΔNBE^{LAG} values, 2007 and 2010—both notably dry years—induced more long-lasting impacts on 2010-2015 ΔNBE^{LAG} (Figure S6). Given the combined importance of short and long-lived impacts of forcing anomalies on lagged effects, we highlight the need to further investigate the relative contributions and potential interactions between single-event lagged effects (e.g. lagged effects attributable to a single forcing anomaly), their longevity, and their net contribution to ΔNBE^{LAG} and ΔNBE IAV.

The decomposition of ΔNBE^{CON} into constituent fluxes—namely net primary productivity (ΔNPP^{CON}), heterotrophic respiration (ΔRHE^{CON}) and fires (ΔFIR^{CON}) —reveals that ΔNPP^{CON} is the largest contributor to ΔNBE^{CON} IAV (Figure 7; Table 4), while ΔFIR^{CON} and ΔNPP^{CON} are comparable contributors to ΔNBE^{CON} in Australia. In northern hemisphere South America and southeast Asia and Indonesia, ΔRHE^{CON} variability is a smaller but substantial contributor to ΔNBE^{CON}, indicating that the integrated impacts of meteorological and disturbance forcing IAV on respiration are comparable to those on photosynthetic uptake. In Australia, the concurrent impact of fires on ΔNBE^{CON} is comparable to ΔNPP^{CON} (Table 4). Similarly, the decomposition of ΔNBE^{LAG} into constituent fluxes (ΔNPP^{LAG}, ΔRHE^{LAG} and ΔFIR^{LAG}), reveals that ΔNBE^{LAG} is ubiquitously dominated by ΔNPP^{LAG} variability, followed by modest contributions from ΔRHE^{LAG} variability and minimal contributions by ΔFIR^{LAG} variability (see Table 4). The prominence of ΔNPP^{LAG} is attributable to faster continental-scale response of C uptake following year-to-year variations in initial C and H_2O states (relative to ΔRHE^{LAG}), indicating that live biomass dynamics (rather than dead organic C states) dominate initial ecosystem responses to external forcing anomalies. The relatively small contribution of ΔFIR^{LAG} values to ΔNBE^{LAG} indicate that the magnitude of fires is, to first order, dominated by variability in the forcing, rather than variability in of fuel load within fire-prone ecosystems.

We find that variability in foliar C, plant-available H_2O and soil C contribute to the majority of regional and pan-tropical ΔNBE^{LAG} variability (Figure 8). For example, both the enhanced foliar C and plant-available H_2O in 2011 over the Australian continent (relative to 2010)—attributable to a combination of reduced fires and increased productivity due to anomalously wet 2010 conditions over the Australian continent (Figure S3)—each contributed to a 0.1PgC/yr net uptake increase (i.e. NBE reduction) relative to 2010. Similarly, we found that reduced foliar C in southern hemisphere South America following dry conditions in 2005, 2007 and 2010 induced a 0.1PgC/yr NBE response in 2006, 2008 and 2011, respectively. We find that the sum of all the pool-specific ΔNBE^{LAG} anomalies approximately add up to ΔNBE^{LAG} (Figure S3), indicating that—insofar as these are represented in DALEC2a—ΔNBE^{LAG} is (a) to first order equivalent to the sum of NBE^{LAG} sensitivities to individual initial states, and (b) cross-pool interactions ("*I*" in Eq. 22) are a secondary component of ΔNBE^{LAG}. In aggregate, we find that foliar C variability contributes to 41-120% of ΔNBE^{LAG} variability across all regions, and 58% of the pan-tropical ΔNBE^{LAG}. Northern hemisphere sub-Saharan Africa and south-east Asia and Indonesia are the only regions where inter-annual variations in soil C and plant-available H_2O (respectively) contribute to more variability than foliar C (Table 5). Notably, our results indicate that under a climatological mean forcing, (a) year-to-year changes in foliar C and plant-available H_2O initial conditions are sufficient to induce substantial year-to-year changes in C uptake, and (b) year-to-year changes in soil C are sufficient to substantially influence total heterotrophic respiration rates; we find that the remaining states (labile C, wood C, fine root C and litter C) explain < 0.2 PgC/yr variability of ΔNBE^{LAG} across all regions. We also find that the sum of regional foliar C and plant-available H_2O impacts on ΔNBE^{LAG} (Figure 8) are approximately equivalent to ΔNPP^{LAG} (Figure 7); in turn, the considerable contributions of both ΔNPP^{LAG} and ΔNPP^{CON} across tropical ecosystems indicates that both climatic variability and initial ecosystem states are substantial contributors to tropical ΔNPP IAV. Inter-annual variations of foliar C, soil C and plant-available H_2O states exhibit substantial correlations to their corresponding ΔNBE^{LAG} components (Figure S5): regional correlations are negative for foliar C (r = -0.6 – -1.0) and plant-available H_2O (r = -0.7 – -0.2), and positive for soil C (r = 0.6 – 1.0). We note that the general agreement between regional 2001-2015 foliar C IAV (1.1 – 4.0%), CARDAMOM LAI IAV (1.6 – 4.8%) and MODIS LAI IAV(0.7– 5.2%) corroborates the estimated impact of CARDAMOM C foliar dynamics on ΔNBE^{LAG}. In contrast to foliar C and plant-available H_2O, soil C impacts on ΔNBE^{LAG} are predominantly induced by long-term soil C trends, rather than year-to-tear variability. Soil C regional trend signs (Figure 7) are generally opposite to mean 2001-2015 NBE signs within each region (Figure 5), indicating that the observed regional C imbalances are substantially mediated by 2001-2015 soil C trends.

Overall, our results indicate that (i) ΔNBE^{LAG} IAV is a prominent component of NBE IAV across tropical ecosystems; (ii) ΔNBE^{LAG} IAV is largely mediated by changes in ecosystem NPP capacity (ΔNPP^{LAG} IAV); and (iii) ΔNPP^{LAG} variability is regulated by inter-annual variations in ecosystem canopy and plant-available H_2O states. In other words, our results highlight that inter-annual changes in ΔNBE—regardless of external forcing anomalies—are substantially determined by inter-annual anomalies in ecosystem H_2O and canopy states. Lagged heterotrophic respiration responses (ΔRHE^{LAG}) are mediated by soil C states changes and are secondary component of NBE IAV; the dampened role of ΔRHE^{LAG} (relative to ΔNPP^{LAG}) is likely

due to the inherent lags between biomass growth and subsequent mortality inputs to soil C states, combined with ~5-50yrs mean dead organic C residence times across tropical ecosystems (Bloom et al., 2016). The relative importance of NPP-mediated lagged effects in responses to climatic anomalies has also been inferred on from in-situ and continental-scale measurements (Sherry et al., 2008, Detmers et al., 2015; Wolf et al., 2016). Our findings also suggest that tracking the long-term evolution of tropical ecosystem canopy cover (Saatchi et al., 2013; Shi et al., 2017) and reducing the process-level uncertainties associated with foliar C dynamics relationships to meteorological and disturbance forcings (discussed in 3.3) are potentially critical for advancing process-level understanding of tropical NBE IAV. We anticipate that continued monitoring of NBE (e.g. following the 2015-2016 ENSO event), and subsequent attribution to concurrent and lagged effects, will also be critical to better quantify the longevity NPP recovery (e.g. Schwalm et al., 2017) and to improve confidence in characterizing concurrent and lagged NPP impacts on the tropical C balance. Finally, while our analysis is focused on the ΔNBE^{LAG} sensitivity to year-to-year ecosystem states changes, we note that the magnitude of ΔNBE^{CON} is also in principle dependent on time-varying ecosystem states (Figure 1); we recognize that further investigation on whether ΔNBE^{CON} IAV is (a) predominantly sensitive to forcing anomalies, or (b) sensitive to year-to-year ecosystem state changes, could amount to a critical step towards accurately characterizing the climate sensitivity of ΔNBE.

3.3 Observation and model uncertainty caveats

The prescribed observation uncertainty characteristics (Table 1) are potentially a critical source of error in the data-informed representation of terrestrial C cycle dynamics and its subsequent partitioning into concurrent and lagged effects. For example, relative differences in the mean NBE values retrieved from aircraft and satellite CO_2 measurements over the Amazon Basin (Alden et al., 2016; Bowman et al. 2017) highlight the need to determine the sensitivity of our results to top-down estimates of NBE. While the uncertainty structures of top-down CO_2 inversion estimates is beyond the scope of our paper, we recognize the need to robustly assess and characterize uncertainties in seasonal and inter-annual variations in NBE. Potential limitations in the linear SIF:GPP assumption include (i) systematic underestimations of afternoon GPP stress, given that the GOSAT overpass time is ~1pm, and (ii) uncharacterized biases emerging from non-linear SIF:GPP under extreme conditions (Verma et al., 2017). We highlight that recent efforts to merge multiple SIF datasets (Zhang et al., 2018), and process-based representations of SIF:GPP (Bacour et al., 2019) can together be used to improve the accuracy of SIF:GPP representation in CARDAMOM. We also note that the CARDAMOM likelihood function (eq. 3) fundamentally assumes all errors are independent; however, commonalities in the derived datasets—such as systematic representation errors across all datasets and transport errors in the GEOS-Chem derived CO_2 and CO emissions—may lead to unrepresented error correlations in the likelihood functions.

We generally acknowledge that more elaborate approaches and a more comprehensive treatment of model and data error characteristics are necessary to understand the contribution of individual data streams error (Keenan et al., 2011; Heald et al.,

2004; MacBean et al., 2016, 2018). Specifically, the explicit and accurate representation of model structural error is critical for both accurate retrievals of physical parameters and accurate model predictions (Brynjarsdottir & O'Hagan, 2014) and solving for error model parameters (Schoups & Vrugt 2010, Xu et al., 2017) is potentially advantageous for physical parameter retrievals and prediction purposes. For example, we note that without an error model structure we cannot explicitly account for cross correlations in the errors between observations or the impacts of heteroscedasticity (Schoups & Vrugt, 2010). While the identification and optimization of an appropriate structural error model is beyond the scope of this manuscript, we highlight this as an important priority for future CARDAMOM analyses.

Unrepresented processes DALEC2a model structure—particularly processes that are potentially substantial contributors to ΔNBE^{CON} and ΔNBE^{LAG}—amount to an additional source of uncertainty in our analysis. Potentially critical processes include time-varying autotrophic respiration (Rowland et al., 2014), plant C allocation and plant mortality, as well as explicit representation of coarse woody debris (Smallman et al., 2017). In particular, given that our results suggest that foliar C is a major contributor to ΔNBE, unrepresented processes relating to tropical leaf phenology may substantially impact the accuracy of lagged effect attribution, including phenological processes regulating leaf onset, leaf lifespan and litterfall seasonality (Chave et al., 2010; Caldararu et al., 2013, Xu et al., 2016), as well as the time-varying allocation regimes (Doughty et al., 2015). Furthermore, while the DALEC2a phenology assumes a time-invariant ratio between LAI and foliar C (i.e. a time-invariant ecosystem-level leaf carbon mass per area), the joint roles of leaf demographics and species distribution on the temporal variability of leaf carbon mass per area could potentially amount to a significant impact on photosynthetic capacity, and subsequently on the variability of ΔNBE^{CON} and ΔNBE^{LAG}. We also highlight year-to-year changes in species composition (such as C_3:C_4 plants) and the temporal dynamics of vegetation and soil nutrients as potential contributors to ΔNBE^{LAG} (Sherry et al., 2008; Schimel et al., 1997) are potentially unrepresented but critical processes, particularly in fire-prone regions (Pellegrini et al., 2018) and nutrient-limited tropical forest ecosystems (Wieder et al. 2015). A potential limitation in CARDAMOM ET estimates is the assumed inherent water-use efficiency relationship between GPP, ET and VPD (eq. B4); recent efforts (Zhou et al., 2015, Boese et al., 2018) advocate for improved parameterizations for semi-empirical GPP:ET relationships, which could ultimately impact the sign and magnitude of inter-annual CARDAMOM ET variations—and the associated plant-available H_2O balance—across tropical ecosystems. Finally, we highlight the need to investigate the sensitivity of our results to the 2001-2015 climatological mean forcing: while to first order the diagnosis of lagged effect anomalies from the mean (rather than absolute values) are insensitive to the reference forcing, further efforts are required to determine whether non-linear impacts of an alternative reference forcing (e.g. a climatological mean forcing based on a 30-year climate normal) may amplify or dampen ΔNBE^{LAG} IAV estimates.

Our continental-scale results indicate that DALEC2a model complexity is adequate to both represent NBE variability and accurately predict NBE outside the training window on a pan-tropical scale (2015), which provides a first-order assessment of the adequacy of the DALEC2a model structure. A notable exception is the substantial underestimation of CARDAMOM 2015

NBE within the northern hemisphere South America region (Figure 5); given the considerable impact of the 2015 ENSO event within the region (Liu et al., 2017), the biased CARDAMOM NBE prediction suggests that either (a) the DALEC2a model structure cannot adequately represent NBE responses to climatic extremes, or (b) the 2010-2013 NBE observational constrains are insufficient to accurately inform the regional DALEC2a states and process parameters. To determine the relative impact of model error, we anticipate that additional insights could be obtained by retrieving ΔNBE^{CON} and ΔNBE^{LAG} based on alternative DALEC model structures (Fox et al., 2009; Smallman et al., 2017). The implementation of DALEC2a assimilation and prediction evaluation across long-term records eddy covariance CO_2 and H_2O fluxes would amount to a useful evaluation of the model structure constrained by multiple data streams (e.g. following Richardson et al., 2010; Keenan et al., 2013; Smallman et al., 2017), and the potential sensitivities of ΔNBE^{CON} and ΔNBE^{LAG} to underlying model structures. While there are currently few tropical ecosystem sites where multi-year NBE constraints are available, we highlight that the analysis of ΔNBE^{CON} and ΔNBE^{LAG} at eddy covariance sites would also benefit from the relative wealth of ancillary site-level repeat measurements of C and H_2O states and fluxes, and would ultimately allow more in-depth evaluation and hypothesis tests on lagged effect processes and their role on ΔNBE dynamics. Finally, to diagnose the potential role of higher-order process interactions on lagged and concurrent effects—such as nutrient limitations, ecosystem demography and explicit representations of carbon-water-energy interactions—we highlight that the ΔNBE^{CON} and ΔNBE^{LAG} attribution methodology introduced here can in principle be applied using higher complexity terrestrial biosphere models (e.g. Huntzinger et al., 2013, 2017; Macbean et al., 2018; Longo et al., 2019).

4. Conclusions

The prominent role of ΔNBE^{LAG} across the tropics throughout 2001-2015 supports our second hypothesis (section 2.5), namely that concurrent and lagged effect variations are comparable on inter-annual timescales. By constraining a diagnostic ecosystem C balance model with an array of terrestrial C cycle observations (LAI, biomass, soil C, SIF, CO-derived fire C emissions and CO2-derived NBE), we show that on annual timescales both ΔNBE^{CON} and ΔNBE^{LAG} effects are substantial contributors to the 2001-2015 tropical C balance. The IAV of ΔNBE^{CON} is largely accounted for by NPP, with sizeable fire contributions from Australia, southeast Asia and Indonesia and South America, and heterotrophic respiration contributions from wet tropical ecosystems. ΔNBE^{LAG} variability is overwhelmingly dominated by the impact of inter-annual variations in lagged NPP effects, followed by a modest contribution from the state-dependence of heterotrophic respiration. In aggregate, anomalies in foliar C, plant-available H_2O, and soil C were identified as the primary influences on ΔNBE^{LAG} variability. Our findings therefore highlight a critical need to explicitly account for lagged effects when investigating the process-level tropical NBE responses to climatic variability on inter-annual timescales. Furthermore, our findings highlight the need to accurately and continuously resolve NBE at sub-continental scales in order to advance our mechanistic and process-level understanding of terrestrial C cycling and its evolving sensitivity to climate.

Appendix A: Regional definitions

Appendix B: Model description

The following sections provide a summary of the process parameterizations introduced in the DALEC version implemented in the Bloom et al., (2016) study. For completeness, a full description of DALEC2a is provided in the manuscript supplement.

B1. DALEC2a Water balance and GPP water stress

The DALEC2a plant-available water balance at timestep *t+1* in is derived as

$$W_{t+1} = W_t + (P_t - R_t - ET_t)\,\Delta t \quad \text{(B1)},$$

where W denotes total plant-available H_2O [in mm H_2O storage equivalent], and P, R and ET precipitation, runoff and evapotranspiration fluxes [mm/day] over the time period Δt [days]. We note that this equation represents a water balance in the dynamic plant-available H_2O pool and does not include deep groundwater, confined aquifers or other unconnected/static storages. Following a generalized non-linear reservoir formulation, we parameterize monthly runoff losses as a second-order decay function with respect to storage, W_t, as:

$$R_t = \alpha W_t^2 \quad \text{(B2)},$$

where α is a second-order decay constant [$mm^{-1}\ day^{-1}$]. The dependence of runoff on W^2—instead of W—ensures that the fractional rate of plant-available H_2O loss is proportional to W; relative to a first-order linear kinetics model, this provides a better representation of faster relative plant-available H_2O depletion following high precipitation events, followed by slower losses during lower precipitation timespans (e.g. Matteucci et al., 2015) and serves a functional approximation of both storage-excess and infiltration-excess runoff generation mechanisms in most cases. Following previous results from land surface model development experiments (e.g. Liang et al., 1994; Lawrence et al., 2011), we assume that net runoff inputs from adjacent pixels are a negligible term in the lumped grid-scale H_2O budget at 4°×5° spatial resolution. By construction, R_t values predicted at $W_t > \frac{1}{a\Delta t}$ are unphysically high ($W_t - R_t\Delta t < 0$), while loss rates at $W_t > \frac{1}{2a\Delta t}$ produce implausibly low residual storage ($W_t - R_t\Delta t$) values. Therefore, in the eventuality of $W_t > \frac{1}{2a\Delta t}$, we calculate runoff as $R_t = W_t - \frac{1}{2a\Delta t}$, effectively represent a storage-excess overflow mechanism by introducing a transition between a state-dependent regime to a direct runoff regime.

We apply a linear scaling on GPP with respect to the plant-available H_2O, where

$$GPP_t = GPP_{\max\,(t)} \max\left(1, \frac{W_t}{\omega}\right) \quad \text{(B3)},$$

where ω represents the plant-available H_2O stress threshold; Eq. B3 effectively imposes a stress factor on GPP spanning between 0 and 1, and offers a simplified representation of the integrated effects of leaf-soil H_2O potential differences and their impact on canopy conductance; Evapotranspiration at time *t* is derived as

$$ET_t = GPP_t \frac{VPD_t}{\upsilon_e} \quad \text{(B4)},$$

where υ_e is the inherent water-use efficiency (Beer et al., 2009) and *VPD* is the vapor pressure deficit derived from ERA-interim monthly reanalysis datasets. Equations B1-B4 amount to a plant-water feedback parameterization, and together represent a reduced complexity version of the DALEC water module implemented by Spadavecchia et al., (2011). All parameters involved in the above-mentioned parameterization—namely α, υ_e, ω and W_0—are optimized along with other DALEC2a parameters in CARDAMOM; the prior ranges are described in Table S1.

B2. Heterotrophic respiration

We parameterize the meteorological dependence of heterotrophic respiration, ρ at time *t* as follows:

$$\rho_t = e^{\Theta(T_t - \overline{T})} \left(\left(\frac{P_t}{\overline{P}} - 1 \right) s_p + 1 \right) \quad \text{(B5)},$$

where *T* and *P* represent the monthly temperature and precipitation vectors. We chose to use *P* as a driver for heterotrophic respiration sensitivity to moisture, given that (a) the majority of heterotrophic respiration is expected to occur in the near-surface soil layer, and (b) near-surface soil moisture strongly covaries with *P*—rather than water storage—at monthly timescales. Previous versions of DALEC solely parameterized ρ_t as a function of temperature (e.g. Bloom et al., 2016 and references therein); effectively, the formulation in Eq. B5 induces a joint sensitivity to relative changes in both temperature and near-surface moisture. The prior ranges for the respiration temperature and precipitation sensitivity parameters (Θ and s_p) are reported in Table S1.

Appendix C: Sensitivity of lagged effects to individual ecosystem states

In the DALEC2a representation of the ecosystem C balance, the state vector $\boldsymbol{x}_a$ consists of the C and H_2O pool values at the start of year *a*. To diagnose the sensitivity of 2010-2015 lagged effects on the variability of ecosystem states, we conduct a sensitivity analysis to explicitly quantify the impact of individual ecosystem state anomalies—relative to their 2010-2015 mean values—on the variability of $\delta\boldsymbol{x}^{LAG}$ throughout 2010-2015. To do this, we define the anomaly of the *n*th individual state in year *a* as the sum of finite differences relative to the mean state:

$$\boldsymbol{x}_a = \overline{\boldsymbol{x}} + \sum_{n=1}^{N}[\boldsymbol{x}_{a(n)} - \overline{\boldsymbol{x}}] \quad \text{(C1)},$$

where $\overline{\boldsymbol{x}}$ is an *N*-element vector of the mean 2010-2015 states; *N* is the number of model state variables; $\boldsymbol{x}_{a(n)}$ is an *N*-element vector of ecosystem states, where for the *i*th element $\boldsymbol{x}_{a(n)}(i) = \boldsymbol{x}_a(i)$ for i = n, and $\boldsymbol{x}_{a(n)}(i) = \overline{\boldsymbol{x}}(i)$ for i≠n. Based on Eq. 11 and Eq.14, we can derive the state change under a climatological mean forcing of each term in Eq. C1, and therefore

$$\delta\boldsymbol{x}_a^{LAG} = \delta\overline{\boldsymbol{x}}^{LAG} + \sum_{n=1}^{N}[\delta\boldsymbol{x}_{a(n)}^{LAG} - \delta\overline{\boldsymbol{x}}^{LAG}] + I_a \quad \text{(C2)};$$

I_a collectively accounts for the unaccounted contribution of higher-order interactions between individual pool anomalies $[\boldsymbol{x}_{a(n)} - \overline{\boldsymbol{x}}]$ on $\delta\boldsymbol{x}_a^{LAG}$. As outlined in section 2.5, the "$\delta\boldsymbol{x}$" terms in Equations C2 can be mapped onto any DALEC2a flux variable; specifically, NBE_a^{LAG} can be defined as the sum of lagged effect *NBE* components attributable to $\delta\boldsymbol{x}_{a(n)}^{LAG}$ and $\delta\overline{\boldsymbol{x}}^{LAG}$ as follows:

$$NBE_a^{LAG} = \overline{NBE}^{LAG} + \sum_{n=1}^{N}[NBE_{a(n)}^{LAG} - \overline{NBE}^{LAG}] + I_a \quad \text{(C3)};$$

$\overline{NBE}^{LAG}$ and $\overline{NBE}_{a(n)}^{LAG}$ can be directly calculated from $D(\overline{\boldsymbol{x}}, \boldsymbol{M}', \boldsymbol{p})$ and $D(\boldsymbol{x}_{a(n)}, \boldsymbol{M}_a, \boldsymbol{p})$, respectively. More succinctly, we summarize Eq. B3 as:

$$NBE_a^{LAG} = \overline{NBE}^{LAG} + \sum_{n=1}^{N}\delta NBE_{a(n)}^{LAG} + I_a \quad \text{(C4)},$$

where $\delta NBE_{a(n)}^{LAG}$ represents the lagged effect anomaly attributable solely to the initial condition anomaly in ecosystem state *n*. By applying the "Δ" operator (Eq. 21) on Eq. C3, eq. C4 can alternatively be expressed as:

$$\Delta NBE_a^{LAG} = \sum_{n=1}^{N}\Delta NBE_{a(n)}^{LAG} + \Delta I_a \quad \text{(C5)}.$$

Effectively, the lagged effect partitioning formulation outlined in Eq. C5 allows us to quantitatively diagnose the *NBE* lagged effect dependence on the inter-annual dynamics of individual C and H_2O states depicted in Figure 2.

Acknowledgments

Part of this work was carried out at the Jet Propulsion Laboratory, California Institute of Technology, under a contract with the National Aeronautics and Space Administration (NASA), supported by NASA Earth Sciences grant (no. NNH16ZDA001N-IDS). Part of this study was funded as a component of NERC's support of the National Centre for Earth Observation. SSS and AGK were also supported by NASA through the Earth Science program. We are thankful for feedback from M. Keller and M. Longo. The NCAR MOPITT project is supported by the National Aeronautics and Space Administration (NASA) Earth Observing System (EOS) Program. The MOPITT team acknowledges the contributions of COMDEV and ABB BOMEM with support from the Canadian Space Agency (CSA), the Natural Sciences and Engineering Research Council (NSERC) and Environment Canada.

Author Contributions

AB, KB, JL, AK, DS designed the research, AB conducted the analysis, all co-authors extensively contributed to evaluation of results and writing of the manuscript.

Competing interests

The authors declare that they have no conflict of interest.

Data availability

ECMWF re-analysis datasets were obtained from www.ecmwf.int. Burned area was obtained from www.globalfiredata.org/. MODIS LAI data were obtained from modis.gsfc.nasa.gov. CMS-Flux datasets are available at cmsflux.jpl.nasa.gov. Biomass is available from Sassan Saatchi (Sasan.S.Saatchi@jpl.nasa.gov) upon reasonable request. The HWSD soil dataset is available at www.fao.org. Gridded GOSAT fluorescence datasets used in this analysis are available from Nicholas Parazoo (nicholas.c.parazoo@jpl.nasa.gov) upon reasonable request. Biomass burning CO fluxes are available from dashrepo.ucar.edu/dataset/CO_Flux_Inversion_Attribution.html. FLUXCOM datasets were obtained from www.fluxcom.org. FLUXSAT GPP was obtained from avdc.gsfc.nasa.gov/pub/tmp/FluxSatGPP. MODIS ET was obtained from http://files.ntsg.umt.edu/data/NTSG_Products/. The NOAA ESRL dataset was obtained from

www.esrl.noaa.gov/gmd/ccgg/trends/. The CARDAMOM results presented in throughout the manuscript analysis are available upon request.

References

Ahlström, A., Raupach, M. R., Schurgers, G., Smith, B., Arneth, A., Jung, M., Reichstein, M., Canadell, J. G., Friedlingstein, P., Jain, A. K., Kato, E., Poulter, B., Sitch, S., Stocker, B. D., Viovy, N., Wang, Y. P., Wiltshire, A., Zaehle, S., and Zeng, N.: The dominant role of semi-arid ecosystems in the trend and variability of the land CO_2 sink, Science, 348, 895–899, 2015.

Alden, C. B., Miller, J. B., Gatti, L. V., Gloor, M. M., Guan, K., Michalak, A. M., van der Laan-Luijkx, I. T., Touma, D., Andrews, A., Basso, L. S., Correia, C. S. C., Domingues, L. G., Joiner, J., Krol, M. C., Lyapustin, A. I., Peters, W., Shiga, Y.P., Thoning, K., van der Velde, I. R., van Leeuwen, T. T., Yadav, V., and Diffenbaugh, N. S.: Regional atmospheric CO_2 inversion reveals seasonal and geographic differences in Amazon net biome exchange, Glob. Change Biology, 22, 3427–3443, https://doi.org/10.1111/gcb.13305, 2016.

Andela, N. and van der Werf, G. R.: Recent trends in African fires driven by cropland expansion and El Niño to La Niña transition, Nature Climate Change, 4, 791–795, 2014.

Anderegg, W.R., Schwalm, C., Biondi, F., Camarero, J.J., Koch, G., Litvak, M., Ogle, K., Shaw, J.D., Shevliakova, E., Williams, A.P., Wolf, A., Ziaco, E., and Pacala, S.: Pervasive drought legacies in forest ecosystems and their implications for carbon cycle models. Science, 349, 528-532, 2015.

Araújo, T.M., Carvalho Jr, J.A., Higuchi, N., Brasil Jr, A.C.P. and Mesquita, A.L.A.: A tropical rainforest clearing experiment by biomass burning in the state of Pará, Brazil. Atmospheric Environment, 33, 1991-1998, 1999.

Arnone, J. A., Verburg, P. S. J., Johnson, D. W., Larsen, J. D., Jasoni, R. L., Lucchesi, A. J., Batts, C. M., von Nagy, C., Coulombe, W. G., Schorran, D. E., Buck, P. E., Braswell, B. H., Coleman, J. S., Sherry, R. A, Wallace, L. L., Luo, Y. and Schimel, D. S.: Prolonged suppression of ecosystem carbon dioxide uptake after an anomalously warm year., Nature, 455, 383–386, doi:10.1038/nature07296, 2008.

Bacour, C., Maignan, F., MacBean, N., Porcar-Castell, A., Flexas, J., Frankenberg, C., Peylin, P., Chevallier, F., Vuichard, N. and Bastrikov, V.: Improving estimates of Gross Primary Productivity by assimilating solar-induced fluorescence satellite retrievals in a terrestrial biosphere model using a process-based SIF model. Journal of Geophysical Research: Biogeosciences, 2019.

Baker, D.F., Law, R.M., Gurney, K.R., Rayner, P., Peylin, P., Denning, A.S., Bousquet, P., Bruhwiler, L., Chen, Y.H., Ciais, P. and Fung, I.Y.: TransCom 3 inversion intercomparison: Impact of transport model errors on the interannual variability of regional CO2 fluxes, 1988–2003. Global Biogeochemical Cycles, 20(1), 2006.

Baldocchi, D., Chu, H., & Reichstein, M.: Inter-annual variability of net and gross ecosystem carbon fluxes: A review. Agricultural and Forest Meteorology, 520-533, 2017.

Bastos, A., Running, S.W., Gouveia, C. and Trigo, R.M.: The global NPP dependence on ENSO: La Niña and the extraordinary year of 2011. Journal of Geophysical Research: Biogeosciences, 118, 1247-1255, 2013.

Beer, C., Ciais, P., Reichstein, M., Baldocchi, D., Law, B. E., Papale, D., Soussana, J. F., Ammann, C., Buchmann, N., Frank,D., Gianelle, D., Janssens, I. A., Knohl, A., Koestner, B., Moors, E., Roupsard, O., Verbeeck, H., Vesala, T., Williams, C. A., and Wohlfahrt, G.: Temporal and among-site variability of inherent water use efficiency at the ecosystem level, Global Biogeochem. Cy., 23, doi:10.1029/2008gb003233, 2009.

Beer, C., Reichstein, M., Tomelleri, E., Ciais, P., Jung, M., Carvalhais, N., Rödenbeck, C., Arain, M. A., Baldocchi, D., Bonan, G. B., Bondeau, A., Cescatti, A., Lasslop, G., Lindroth, A., Lomas, M., Luyssaert, S., Margolis, H., Oleson, K. W., Roupsard, O., Veendendaal, E., Viovy, N., Williams, C., Woodard, F. I., and Papale, D.: Terrestrial gross cabon dioxide uptake: Global distribution and covariation with climate, Science, 329, 834–838, doi:10.1126/science1184984, 2010.

Bi, J., Knyazikhin, Y., Choi, S., Park, T., Barichivich, J., Ciais, P., Fu, R., Ganguly, S., Hall, F., Hilker, T. and Huete, A.: Sunlight mediated seasonality in canopy structure and photosynthetic activity of Amazonian rainforests. Environmental Research Letters, 10, 064014, 2015.

Bloom, A. A. and Williams, M.: Constraining ecosystem carbon dynamics in a data-limited world: integrating ecological "common sense" in a model–data fusion framework, Biogeosciences, 12, 1299–1315, https://doi.org/10.5194/bg-12-1299-2015, 2015.

Bloom, A. A., Worden, J., Jiang, Z., Worden, H., Kurosu, T., Frankenberg, C., and Schimel, D.: Remote sensing constraints on South America fire traits by Bayesian fusion of atmospheric and1140 surface data, Geophys. Res. Lett., 42, 1268–1274, doi:10.1002/2014GL062584, 2015.

Bloom, A. A., Exbrayat, J.-F., van der Velde, I. R., Feng, L., and Williams., M.: The decadal state of the terrestrial carbon cycle: Global retrievals of terrestrial carbon allocation, pools, and residence times, P. Natl. Acad. Sci. USA, 113, 1285–1290, https://doi.org/10.1073/pnas.1515160113, 2016.

Bloom, A. Anthony, Jiang, Zhe, Worden, Helen: Global Carbon Monoxide (CO) Flux Estimates for 2001-2015. UCAR/NCAR - DASH Repository. https://doi.org/10.26024/r1r2-6620., 2019.

Boese, S., Jung, M., Carvalhais, N., and Reichstein, M.: The importance of radiation for semiempirical water-use efficiency models, Biogeosciences, 14, 3015–3026, https://doi.org/10.5194/bg-14-3015-2017, 2017.

Bowman, K.W., Liu, J., Bloom, A.A., Parazoo, N.C., Lee, M., Jiang, Z., Menemenlis, D., Gierach, M.M., Collatz, G.J., Gurney, K.R. and Wunch, D.: Global and Brazilian carbon response to El Niño Modoki 2011–2010. Earth and Space Science, 4, 637-660, 2017

Braswell, B.H., Schimel, D.S., Linder, E. and Moore, B.I.I.I.: The response of global terrestrial ecosystems to interannual temperature variability. Science, 278, 870–873, 1997.

Brynjarsdóttir, J., and O'Hagan., A.: Learning about physical parameters: The importance of model discrepancy." Inverse Problems 30.11: 114007, 2014.

Caldararu, S., Palmer, P. I., and Purves, D. W.: Inferring Amazon leaf demography from satellite observations of leaf area index, Biogeosciences, 9, 1389–1404, doi:10.5194/bg-9-1389- 2012, 2012.

Carvalhais, N., Forkel, M., Khomik, M., Bellarby, J., Jung, M., Migliavacca, M., Mu, M., Saatchi, S., Santoro, M., Thurner, M., Weber, U., Ahrens, B., Beer, C., Cescatti, A., Randerson, J. T., and Reichstein, M.: Global covariation of carbon turnover times with climate in terrestrial ecosystems, Nature, 514, 213–217, https://doi.org/10.1038/nature13731, 2014.

Chave,J.,Navarrete,D.,Almeida,S.,Álvarez,E., Aragão,L.E.O. C., Bonal, D., Châtelet, P., Silva-Espejo, J. E., Goret, J.-Y., von Hildebrand, P., Jiménez, E., Patiño, S., Peñuela, M. C., Phillips, O. L., Stevenson, P., and Malhi, Y.: Regional and seasonal pat- terns of litterfall in tropical South America, Biogeosciences, 7, 43–55, doi:10.5194/bg-7-43-2010, 2010.

Chen, Y., Morton, D. C., Jin, Y., Collatz, G. J., Kasibhatla, P. S., Werf, G. R. van der, DeFries, R. S., and Randerson, J. T.: Long-term trends and interannual variability of forest, savanna and agricultural fires in South America, Carbon Managment, 4, 617–638, doi:10.4155/cmt.13.61, 2013.

Cox, P., Pearson, D., Booth, B., Friedlingstein, P., Huntingford, C., Jones, C., and Luke, C.: Sensitivity of tropical carbon to climate change constrained by carbon dioxide variability, Nature, 494, 341–344, 2013.

Deeter, M. N., Martínez-Alonso, S., Edwards, D. P., Emmons, L. K., Gille, J. C., Worden, H. M., Sweeney, C., Pittman, J. V., Daube, B. C., and Wofsy, S. C.: The MOPITT Version 6 product: algorithm enhancements and validation, Atmos. Meas. Tech., 7, 3623–3632, doi:10.5194/amt-7-3623-2014, 2014.

Desai, A.R.: Climatic and phenological controls on coherent regional interannual variability of carbon dioxide flux in a heterogeneous landscape. Journal of Geophysical Research: Biogeosciences, 115(G3), 2010.

Detmers, R. G., Hasekamp, O., Aben, I., Houweling, S., Leeuwen, T. T. V., Butz, A., Landgraf, J., Köhler, P., Guanter, L. and Poulter, B.: Anomalous carbon uptake in Australia as seen by GOSAT, Geophys. Res. Lett., 42, 8177–8184, doi:10.1002/2015GL065161, 2015.

Doughty, C. E., Metcalfe, D. B., Girardin, C. A. J., Amezquita,F. F., Durand, L., Huasco, W. H., Costa, M. C., Costa, A. C. L., Rocha, W., Meir, P., Galbraith, D., and Malhi, Y.: Source and sink carbon dynamics and carbon allocation in the Amazon basin, Global Biogeochemical Cycles, 1–11, 2015.

Exbrayat, J.-F., Pitman, A. J., Zhang, Q., Abramowitz, G., and Wang, Y.-P.: Examining soil carbon uncertainty in a global model: response of microbial decomposition to temperature, moisture and nutrient limitation, Biogeosciences, 10, 7095– 7108, https://doi.org/10.5194/bg-10-7095-2013, 2013a.

Exbrayat, J.F., Pitman, A.J., Abramowitz, G. and Wang, Y.P.,: Sensitivity of net ecosystem exchange and heterotrophic respiration to parameterization uncertainty. Journal of Geophysical Research: Atmospheres, 118(4), pp.1640-1651, 2013b.

Exbrayat, J.F., Smallman, T.L., Bloom, A.A., Hutley, L.B. and Williams, M.: Inverse determination of the influence of fire on vegetation carbon turnover in the pantropics. Global Biogeochemical Cycles, 32, 1776-1789, 2018.

Falloon, P., Jones, C. D., Ades, M., & Paul, K.: Direct soil moisture controls of future global soil carbon changes : An important source of uncertainty. Global Biogeochem.Cycles, 25, GB3010, 2011.

Fang, Y., Michalak, A. M., Schwalm, C. R., Huntzinger, D. N., Berry, J. A., Ciais, P., Piao, S. L., Poulter, B., Fisher, J. B., Cook, R. B., Hayes, D., Huang, M. Y., Ito, A., Jain, A., Lei, H. M., Lu, C. Q., Mao, J. F., Parazoo, N. C.,

Peng, S. S., Ricciuto, D. M., Shi, X. Y., Tao, B., Tian, H. Q., Wang, W. L., Wei, Y. X., and Yang, J.: Global land carbon sink response to temperature and precipitation varies with ENSO phase, Environmental Research Letters, 12, 064007, https://doi.org/10.1088/1748-9326/aa6e8e, 2017.

Feng, L., Palmer, P. I., Bösch, H., Parker, R. J., Webb, A. J., Cor- reia, C. S. C., Deutscher, N. M., Domingues, L. G., Feist, D. G., Gatti, L. V., Gloor, E., Hase, F., Kivi, R., Liu, Y., Miller, J. B., Morino, I., Sussmann, R., Strong, K., Uchino, O., Wang, J., and Zahn, A.: Consistent regional fluxes of CH_4 and CO_2 inferred from GOSAT proxy XCH_4:XCO_2 retrievals, 2010–2014, At- mos. Chem. Phys., 17, 4781–4797, https://doi.org/10.5194/acp- 17-4781-2017, 2017.

Fox, A., Williams, M., Richardson, A. D., Cameron, D., Gove, J. H., Quaife, T., Ricciuto, D., Reichstein, M., Tomelleri, E., Trudinger, C. M., and van Wijk, M. T.: The reflex project: comparing different algorithms and implementations for the inversion of a terrestrial ecosystem model against eddy covariance data, Agricultural and Forest Meteorology, 149, 1597–1615, 2009.

Frank, D., Reichstein, M., Bahn, M., Thonicke, K., Frank, D., Mahecha, M., Smith, P., Van der Velde, M., Vicca, S., Babst, F., Beer, C., Buchmann, N., Canadell, J., Ciais, P., Cramer, W., Ibrom, A., Miglietta, F., Poulter, B., Rammig, A., Seneviratne, S., Walz, A., Wattenbach, M., Zavala, M., and Zscheischler, J.: Effects of climate extremes on the terrestrial carbon cycle: concepts, processes and potential future impacts, Glob. Change Biol., 21, 7861–2880, 2015.

Frankenberg, C., Fisher, J. B., Worden, J., Badgley, G., Saatchi, S. S., Lee, J.-E., Toon, G. C., Butz, A., Jung, M.,Kuze, A., and Yokota, T.: New global observations of the terrestrial carbon cycle from GOSAT: patterns of plant fluorescence with gross primary productivity, Geophys. Res. Lett., 38, L17706, doi: 10.1029/2011GL048738, 2011.

Friedlingstein, P., Meinshausen, M., Arora, V.K., Jones, C.D., Anav, A., Liddicoat, S.K. and Knutti, R.: Uncertainties in CMIP5 climate projections due to carbon cycle feedbacks. Journal of Climate, 27, 511-526, 2014.

Friend, A. D., Lucht, W., Rademacher, T. T., Keribin, R., Betts, R., Cadule, P., Ciais, P., Clark, D. B., Dankers, R., Fal- loon, P. D., Ito, A., Kahana, R., Kleidon, A., Lomas, M. R., Nishina, K., Ostberg, S., Pavlick, R., Peylin, P., Schaphoff, S., Vuichard, N., Warszawski, L., Wiltshire, A., and Woodward, F. I.: Carbon residence time dominates uncertainty in terrestrial vegetation responses to future climate and atmospheric CO_2, P. Natl. Acad. Sci. USA, 111, 3280–3285, https://doi.org/10.1073/pnas.1222477110, 2014.

Gatti, L. V., Gloor, M., Miller, J. B., Doughty, C. E., Malhi, Y., Domingues, L. G., Basso, L. S., Martinewski, A., Correia, C. S., C., Borges, V. F., Freitas, S., Braz, R., Anderson, L. O., Rocha, H., Grace, J., Phillips, O. L., and Lloyd, J.:

Drought sensitivity of Amazonian carbon balance revealed by atmospheric measurements, Nature, 506, 76–80, doi:10.1038/nature12957, 2014.

Giglio, L., Randerson, J. T., and van der Werf, G. R.: Analysis of daily, monthly, and annual burned area using the fourth-generation global fire emissions database (GFED4), Journal of Geophysical Research Biogeosciences, 118, 317–328, https://doi.org/10.1002/jgrg.20042, 2013.

Guenet, B., Camino-Serrano, M., Ciais, P., Tifafi, M., Maignan, F., Soong, J.L. and Janssens, I.A., 2018. Impact of priming on global soil carbon stocks. Global change biology, 24, 1873-1883, 2018.

Hhhh

Haario, H., Saksman, E. and Tamminen, J.: An adaptive Metropolis algorithm. Bernoulli, 7(2), pp.223-242. 2001

Heald, C.L., Jacob, D.J., Jones, D., Palmer, P.I., Logan, J.A., Streets, D.G., Sachse, G.W., Gille, J.C., Hoffman, R.N. and Nehrkorn, T.: Comparative inverse analysis of satellite (MOPITT) and aircraft (TRACE-P) observations to estimate Asian sources of carbon monoxide. Journal of Geophysical Research: Atmospheres, 109, 2004.

Hiederer, R. and M. Köchy: Global soil organic carbon estimates and the harmonized world soil database, EUR, 79, 25225, doi:10.2788/13267, 2011.

Holling, C.S.: Resilience and stability of ecological systems. Annual review of ecology and systematics, 4(1), pp.1-23, 1973.

Hopkins, F. M., Filley, T. R., Gleixner, G., Lange, M., Top, S. M., & Trumbore, S. E.: Increased belowground carbon inputs and warming promote loss of soil organic carbon through complementary microbial responses. Soil Biology and Biochemistry, 76, 57-69, 2014.

Huntzinger, D. N., Schwalm, C., Michalak, A. M., Schaefer, K., King, A. W., Wei, Y., Jacobson, A., Liu, S., Cook, R. B., Post, W. M., Berthier, G., Hayes, D., Huang, M., Ito, A., Lei, H., Lu, C., Mao, J., Peng, C. H., Peng, S., Poulter, B., Riccuito, D., Shi, X., Tian, H., Wang, W., Zeng, N., Zhao, F., and Zhu, Q.: The North American Carbon Program Multi-Scale Synthesis and Terrestrial Model Intercomparison Project – Part 1: Overview and experimental design, Geosci. Model Dev., 6, 2121–2133, https://doi.org/10.5194/gmd-6-2121-2013, 2013.

Huntzinger, D. N., Michalak, A. M., Schwalm, C., Ciais, P., King, A. W., Fang, Y., Schaefer, K., Wei, Y., Cook, R. B., Fisher, J. B., Hayes, D., Huang, M., Ito, A., Jain, A. K., Lei, H., Lu, C., Maignan, F., Mao, J., Parazoo, N., Peng, S., Poulter, B.,

Ricciuto, D., Shi, X., Tian, H., Wang, W., Zeng, N., and Zhao, F.: Uncertainty in the response of terrestrial carbon sink to environmental drivers undermines carbon-climate feedback predictions, Sci. Rep.-UK, 7, 4765, https://doi.org/10.1038/s41598- 017-03818-2, 2017.

Jiang, Z., Worden, J.R., Worden, H., Deeter, M., Jones, D., Arellano, A.F. and Henze, D.K.: A 15-year record of CO emissions constrained by MOPITT CO observations. Atmospheric Chemistry and Physics, 17(7), 2017.

Joiner, J., Yoshida, Y., Zhang, Y., Duveiller, G., Jung, M., Lyapustin, A., Wang, Y. and Tucker, C.J.: Estimation of terrestrial global gross primary production (GPP) with satellite data-driven models and eddy covariance flux data. *Remote Sensing*, *10*(9), p.1346, 2018.

Jung, M., Reichstein, M., Schwalm, C. R., Huntingford, C., Sitch, S., Ahlström, A., Arneth, A., Camps-Valls, G., Ciais, P., Friedlingstein, P., Gans, F., Ichii, K., Jain, A. K., Kato, E., Papale, D., Poulter, B., Raduly, B., Rödenbeck, C., Tramontana, G., Viovy, N., Wang, Y.-P., Weber, U., Zaehle, S., and Zeng, N.: Compensatory water effects link yearly global land CO_2 sink changes to temperature, Nature, 541, 516–520, 2017.

Jung, M., Koirala, S., Weber, U., Ichii, K., Gans, F., Camps-Valls, G., Papale, D., Schwalm, C., Tramontana, G. and Reichstein, M.: The FLUXCOM ensemble of global land-atmosphere energy fluxes. Scientific data, 6(1), pp.1-14, 2019.

Jung, M., Schwalm, C., Migliavacca, M., Walther, S., Camps-Valls, G., Koirala, S., Anthoni, P., Besnard, S., Bodesheim, P., Carvalhais, N., Chevallier, F., Gans, F., Goll, D. S., Haverd, V., Köhler, P., Ichii, K., Jain, A. K., Liu, J., Lombardozzi, D., Nabel, J. E. M. S., Nelson, J. A., O'Sullivan, M., Pallandt, M., Papale, D., Peters, W., Pongratz, J., Rödenbeck, C., Sitch, S., Tramontana, G., Walker, A., Weber, U., and Reichstein, M.: Scaling carbon fluxes from eddy covariance sites to globe: synthesis and evaluation of the FLUXCOM approach, Biogeosciences, 17, 1343–1365, https://doi.org/10.5194/bg-17-1343-2020, 2020.

Keenan, T.F., Carbone, M.S., Reichstein, M. and Richardson, A.D.: The model–data fusion pitfall: assuming certainty in an uncertain world. Oecologia, 167, 587, 2011.

Keenan, T. F., Davidson, E. A., Munger, J. W., and Richard- son, A. D.: Rate my data: quantifying the value of ecological data for the development of models of the terrestrial carbon cy- cle, Ecol. Appl., 23, 273–286, 2013.

Kurc, S.A. and Small, E.E.: Soil moisture variations and ecosystem-scale fluxes of water and carbon in semiarid grassland and shrubland. Water Resources Research, 43, 2007.

Lawrence, D.M., K.W. Oleson, M.G. Flanner, P.E. Thornton, S.C. Swenson, P.J. Lawrence, X. Zeng, Z.-L. Yang, S. Levis, K. Sakaguchi, G.B. Bonan, and A.G. Slater, 2011: Parameterization improvements and functional and structural advances in version 4 of the Community Land Model. J. Adv. Model. Earth Sys., 3, DOI: 10.1029/2011MS000045.

Le Quéré, C., Moriarty, R., Andrew, R. M., Canadell, J. G., Sitch, S., Korsbakken, J. I., Friedlingstein, P., Peters, G. P., Andres, R. J., Boden, T. A., Houghton, R. A., House, J. I., Keeling, R. F., Tans, P., Arneth, A., Bakker, D. C. E., Barbero, L., Bopp, L., Chang, J., Chevallier, F., Chini, L. P., Ciais, P., Fader, M., Feely, R. A., Gkritzalis, T., Harris, I., Hauck, J., Ilyina, T., Jain, A. K., Kato, E., Kitidis, V., Klein Goldewijk, K., Koven, C., Landschützer, P., Lauvset, S. K., Lefèvre, N., Lenton, A., Lima, I. D., Metzl, N., Millero, F., Munro, D. R., Murata, A., Nabel, J. E. M. S., Nakaoka, S., Nojiri, Y., O'Brien, K., Olsen, A., Ono, T., Pérez, F. F., Pfeil, B., Pierrot, D., Poulter, B., Rehder, G., Rödenbeck, C., Saito, S., Schuster, U., Schwinger, J., Séférian, R., Steinhoff, T., Stocker, B. D., Sutton, A. J., Takahashi, T., Tilbrook, B., van der Laan-Luijkx, I. T., van der Werf, G. R., van Heuven, S., Vandemark, D., Viovy, N., Wiltshire, A., Zaehle, S., and Zeng, N.: Global Carbon Budget 2015, Earth Syst. Sci. Data, 7, 349–396, https://doi.org/10.5194/essd-7-349-2015, 2015.

Lewis, S. L., Brando, P. M., Phillips, O. L., van der Heijden, G. M. F., and Nepstad, D.: The 2010 Amazon drought, Science, 6017, 554, doi: 10.1126/science.1200807, 2011.

Liang, X., D. P. Lettenmaier, E. F. Wood, and S. J. Burges, 1994: A Simple hydrologically Based Model of Land Surface Water and Energy Fluxes for GSMs, J. Geophys. Res., 99(D7), 14,415-14,428.

Liu, J., Bowman, K. W., Lee, M., Henze, D. K., Bousserez, N., Brix, H., Collatz, G. J., Menemenlis, D., Ott, L., Pawson, S., Jones, D., and Nassar, R.: Carbon monitoring system flux estimation and attribution: impact of ACOS-GOSAT XCO2 sampling on the inference of terrestrial biospheric sources and sinks, Tellus B, 66, 22486, doi:10.3402/tellusb.v66.22486, 2014.

Liu, J., Bowman, K. W., Schimel, D. S., Parazoo, N. C., Jiang, Z., Lee, M., Bloom, A. A., Wunch, D., Frankenberg, C., Sun, Y., O'Dell, C. W., Gurney, K. R., Menemenlis, D., Gierach, M., Crisp, D., and Eldering, A.: Contrasting carbon cycle responses of the tropical continents to the 2015–2016 El Niño, Science, 358, pp. 7, 2017.

Liu, J., Bowman, K., Parazoo, N.C., Bloom, A.A., Wunch, D., Jiang, Z., Gurney, K.R. and Schimel, D.: Detecting drought impact on terrestrial biosphere carbon fluxes over contiguous US with satellite observations. Environmental Research Letters, 13(9), p.095003, 2018.

Longo, M., Knox, R. G., Medvigy, D. M., Levine, N. M., Dietze, M. C., Kim, Y., Swann, A. L. S., Zhang, K., Rollinson, C. R., Bras, R. L., Wofsy, S. C., and Moorcroft, P. R.: The biophysics, ecology, and biogeochemistry of functionally diverse, vertically and horizontally heterogeneous ecosystems: the Ecosystem Demography model, version 2.2 – Part 1: Model description, Geosci. Model Dev., 12, 4309–4346, https://doi.org/10.5194/gmd-12-4309-2019, 2019.

Lovenduski, N.S. and Bonan, G.B.: Reducing uncertainty in projections of terrestrial carbon uptake. Environmental Research Letters, 12(4), p.044020, 2017.

Luo, Y.: Terrestrial carbon cycle feedback to climate warming, Annu. Rev. Ecol. Evol. S., 38, 683–712, doi:10.1146/annurev.ecosys.38.091206.095808, 2007.

Luo, Y. and Weng, E. Dynamic disequilibrium of the terrestrial carbon cycle under global change. Trends in Ecology & Evolution, 26, pp.96-104, 2011.

Luo, Y., Keenan, T.F. and Smith, M.: Predictability of the terrestrial carbon cycle. Global change biology, 21, pp.1737-1751, 2015.

MacBean, N., Peylin, P., Chevallier, F., Scholze, M. and Schuermann, G.: Consistent assimilation of multiple data streams in a carbon cycle data assimilation system. Geoscientific Model Development, 9, 3569-3588, 2016.

MacBean, N., Maignan, F., Bacour, C., Lewis, P., Peylin, P., Guanter, L., Köhler, P., Gómez-Dans, J. and Disney, M.: Strong constraint on modelled global carbon uptake using solar-induced chlorophyll fluorescence data. Scientific reports, 8, 1973, 2018.

Magney, T.S., Frankenberg, C., Fisher, J.B., Sun, Y., North, G.B., Davis, T.S., Kornfeld, A. and Siebke, K.: Connecting active to passive fluorescence with photosynthesis: A method for evaluating remote sensing measurements of Chl fluorescence. New Phytologist, 215(4), pp.1594-1608, 2017.

Matteucci, M., Gruening, C., Ballarin, I.G., Seufert, G. and Cescatti, A.: Components, drivers and temporal dynamics of ecosystem respiration in a Mediterranean pine forest. Soil Biology and Biochemistry, 88, 224-235, 2015.

Moyano, F.E., Manzoni, S. and Chenu, C.,: Responses of soil heterotrophic respiration to moisture availability: An exploration of processes and models. Soil Biology and Biochemistry, 59, pp.72-85, 2013.

Mu, Q., Zhao, M., & Running, S. W.: Improvements to a MODIS global terrestrial evapotranspiration algorithm. Remote sensing of environment, 115(8), 1781-1800, 2011.

Mystakidis, S., Davin, E. L., Gruber, N., & Seneviratne, S. I.: Constraining future terrestrial carbon cycle projections using observation-based water and carbon flux estimates. Global change biology, 22, 6, 2198-2215, 2016.

Parazoo, N.C., Bowman, K., Fisher, J.B., Frankenberg, C., Jones, D.B., Cescatti, A., Pérez-Priego, Ó., Wohlfahrt, G. and Montagnani, L.: Terrestrial gross primary production inferred from satellite fluorescence and vegetation models. Global change biology, 20, 3103-3121, 2014.

Pellegrini, A.F., Ahlström, A., Hobbie, S.E., Reich, P.B., Nieradzik, L.P., Staver, A.C., Scharenbroch, B.C., Jumpponen, A., Anderegg, W.R., Randerson, J.T. and Jackson, R.B.: Fire frequency drives decadal changes in soil carbon and nitrogen and ecosystem productivity. Nature, 553, 194, 2018.

Piao, S., Wang, X., Wang, K., Li, X., Bastos, A., Canadell, J.G., Ciais, P., Friedlingstein, P. and Sitch, S., 2019. Interannual variations of terrestrial carbon cycle: Issues and perspectives. Global change biology, doi:10.1111/gcb.14884, 2019.

Poulter, B., Frank, D., Ciais, P., Myneni, R. B., Andela, N., Bi, J., Broquet, G., Canadell, J. G., Chevallier, F., Liu, Y. Y., Running, S. W., Sitch, S., and van der Werf, G. R.: Contribution of semi- arid ecosystems to interannual variability of the global carbon cycle, Nature, 509, 600–603, 2014.

Powell, T. L., Galbraith, D. R., Christoffersen, B. O., Harper, A., Imbuzeiro, H. M., Rowland, L., Almeida, S., Brando, P. M., da Costa, A. C., Costa, M. H., Levine, N. M., Malhi, Y., Saleska, S. R., Sotta, E., Williams, M., Meir, P., and Moorcroft, P. R.: Confronting model predictions of carbon fluxes with measurements of Amazon forests subjected to experimental drought, New Phytol., 200, 350–365, doi:10.1111/nph.12390, 2013.

Quetin, G.R., Bloom, A.A., Bowman, K.W. and Konings, A.G.: Carbon flux variability from a relatively simple ecosystem model with assimilated data is consistent with terrestrial biosphere model estimates. Journal of Advances in Modeling Earth Systems, 12(3), p.e2019MS001889, 2020.

Randerson, J., van der Werf, G. R., Collatz, G. J., Giglio, L., Still, C. J., Kasibhatla, P., Miller, J. B., White, J. W. C., DeFries, R. S., and Kasischke, E. S.: Fire emissions from C3 and C4 vegetation and their influence on interannual variability of atmospheric CO2 and δ13 CO2, Global Biogeochem. Cy., 19, GB2019, doi:10.1029/2004GB002366, 2005.

Reichstein, M., Bahn, M., Ciais, P., Frank, D., Mahecha, M. D.,Seneviratne, S. I., Zscheischler, J., Beer, C., Buchmann, N.,Frank, D. C., Papale, D., Rammig, A., Smith, P., Thonicke, K., van der Velde, M., Vicca, S., Walz, A., and Wattenbach, M.: Climate extremes and the carbon cycle, Nature, 500, 287–295,doi:10.1038/Nature12350, 2013.

Richardson, A.D., Hollinger, D.Y., Aber, J.D., Ollinger, S.V. and Braswell, B.H.: Environmental variation is directly responsible for short-but not long-term variation in forest-atmosphere carbon exchange. Global Change Biology, 13, pp.788-803, 2007.

Richardson, A. D., Williams, M., Hollinger, D. Y., Moore, D. J., Dail, D. B., Davidson, E. A., Scott, N. A., Evans, R. S., Hughes, H., Lee, J. T., Rodrigues, C., and Savage, K.: Estimating parameters of a forest ecosystem C model with measurements of stocks and fluxes as joint constraints, Oecologia, 164, 25–40, 2010.

Rowland, L., Hill, T.C., Stahl, C., Siebicke, L., Burban, B., Zaragoza-Castells, J., Ponton, S., Bonal, D., Meir, P. and Williams, M.: Evidence for strong seasonality in the carbon storage and carbon use efficiency of an Amazonian forest. Global change biology, 20, 979-991, 2014

Rowland, L., da Costa, A.C.L., Galbraith, D.R., Oliveira, R.S., Binks, O.J., Oliveira, A.A.R., Pullen, A.M., Doughty, C.E., Metcalfe, D.B., Vasconcelos, S.S., Ferreira, L.V., Malhi, Y., Grace, J., Mencuccini, M., and Meir, P.: Death from drought in tropical forests is triggered by hydraulics not carbon starvation. Nature, 528, 119, 2015.

Saatchi, S. S., Harris, N. L., Brown, S., Lefsky, M., Mitchard, E. T., Salas, W., Zutta, B. R., Buermann, W., Lewis, S. L., Hagen, S., Petrova, S., White, L., Silman, M., and Morel, A.: Benchmark map of forest carbon stocks in tropical regions across three continents, P. Natl. Acad. Sci., 108, 9899–9904, 2011.

Saatchi, S., Asefi-Najafabady, S., Malhi, Y., Aragao, L. E. O. C., Anderson, L. O., Myneni, R. B., and Nemani, R.: Persistent effects of a severe drought on Amazonian forest canopy, P. Natl. Acad. Sci. USA, 110, 565–570, 2013.

Schimel, D. S., Braswell, B., Holland, E. A., McKeown, R., Ojima, D., Painter, T. H., Parton, W. J., and Townsend, A. R.: Climatic, edaphic, and biotic controls over storage and turnover of carbon in soils, Global Biogeochem. Cy., 8, 279–293, 1994.

Schimel, D.S., Braswell, B.H., McKeown, R., Ojima, D.S., Parton, W.J. and Pulliam, W.: Climate and nitrogen controls on the geography and timescales of terrestrial biogeochemical cycling. Global Biogeochemical Cycles, 10, pp.677-692, 1996.

Schimel, D. S., Braswell, B. H., and Parton W. J.: Equilibration of the terrestrial water, nitrogen, and carbon cycles, P. Natl. Acad. Sci. USA., 94, 8280–8283, 1997.

Schimel, D., Churkina, G., and Braswell, B.: Remembrance of weather past: ecosystem response to climate variability, in: A history of atmospheric CO_2 and its effects on plants, animals, and ecosystems, edited by: Ehleringer, J. R., Cerling, T. E., and Dearing, M. D., 350–368, Springer-Verlag, Berlin, 2005.

Schoups, G. and Vrugt, J.A.: A formal likelihood function for parameter and predictive inference of hydrologic models with correlated, heteroscedastic, and non-Gaussian errors. Water Resources Research, 46(10), 2010.

Schwalm, C. R., Anderegg, W. R., Michalak, A. M., Fisher, J. B., Biondi, F., Koch, G., Litvak, M., Ogle, K., Shaw, J. D., Wolf, A., Huntzinger, D. N., Schaefer, K., Cook, R., Wei, Y., Fang, Y., Hayes, D., Huang, M., Jain, A., and Tian, H.: Global patterns of drought recovery, Nature, 548, 202–205, 2017.

Sellers, P.J., Schimel, D.S., Moore, B., Liu, J. and Eldering, A.: Observing carbon cycle–climate feedbacks from space. Proceedings of the National Academy of Sciences, 115(31), pp.7860-7868, 2018.

Shea, R. W., Shea, B. W., Kauffman, J. B., Ward, D. E., Haskins, C. I., & Scholes, M. C.: Fuel biomass and combustion factors associated with fires in savanna ecosystems of South Africa and Zambia. Journal of Geophysical Research: Atmospheres, 101, 23551-23568, 1996.

Sherry, R. A., Weng, E., Arnone III, J. A., Johnson, D. W., Schimel, D. S., Verburg, P. S., Wallace, L. L., and Luo, Y.: Lagged effects of experimental warming and doubled precipitation on annual and seasonal aboveground biomass production in a tallgrass prairie, Glob. Change Biol., 14, 2923–2936, 2008.

Shi, M., Liu, J., Zhao, M., Yu, Y. and Saatchi, S.: Mechanistic Processes Controlling Persistent Changes of Forest Canopy Structure After 2005 Amazon Drought. Journal of Geophysical Research: Biogeosciences, 122, 3378-3390, 2017.

Sierra, C. A., Trumbore, S. E., Davidson, E. A., Vicca, S., & Janssens, I.: Sensitivity of decomposition rates of soil organic matter with respect to simultaneous changes in temperature and moisture. Journal of Advances in Modeling Earth Systems, 7, 335–356, 2015.

Smallman, T. L., Exbrayat, J.-F., Mencuccini, M., Bloom, A. A., and Williams, M.: Assimilation of repeated woody biomass observations constrains decadal ecosystem carbon cycle uncertainty in aggrading forests, J. Geophys. Res.-Biogeo., 122, 528–545, https://doi.org/10.1002/2016JG003520, 2017.

Smith, M.D., Knapp, A.K. and Collins, S.L.: A framework for assessing ecosystem dynamics in response to chronic resource alterations induced by global change. Ecology, 90, 3279-3289, 2009.

Spadavecchia, L., Williams, M. and Law, B.E.: Uncertainty in predictions of forest carbon dynamics: separating driver error from model error. Ecological Applications, 21,1506-1522, 2011.

Sun, Y., Frankenberg, C., Wood, J.D., Schimel, D.S., Jung, M., Guanter, L., Drewry, D.T., Verma, M., Porcar-Castell, A., Griffis, T.J. and Gu, L.: OCO-2 advances photosynthesis observation from space via solar-induced chlorophyll fluorescence. Science, 358(6360), p.eaam5747, 2017.

Takagi, H., Houweling, S., Andres, R. J., Belikov, D., Bril, A., Boesch, H., Butz, A., Guerlet, S., Hasekamp, O., Maksyutov, S., Morino, I., Oda, T., O'Dell, C. W., Oshchepkov, S., Parker, R., Saito, M., Uchino, O., Yokota, T., Yoshida, Y., and Valsala, V.: Influence of differences in current GOSAT XCO_2 retrievals on surface flux estimation, Geophysical Research Letters, 41, 2598–2605, doi:10.1002/2013GL059174, 2014.

Thompson, M.V., Randerson, J.T., Malmström, C.M. and Field, C.B.: Change in net primary production and heterotrophic respiration: How much is necessary to sustain the terrestrial carbon sink? Global Biogeochemical Cycles, 10, 711-726, 1996.

Trumbore, S.: Carbon respired by terrestrial ecosystems–recent progress and challenges. Global Change Biology, 12,.141-153, 2006.

van der Werf, G. R., Randerson, J. T., Giglio, L., Collatz, G. J., Mu, M., Kasibhatla, P. S., Morton, D. C., DeFries, R. S., Jin, Y., and van Leeuwen, T. T.: Global fire emissions and the contribution of deforestation, savanna, forest, agricultural, and peat fires (1997–2009), Atmos. Chem. Phys., 10, 11707-11735, https://doi.org/10.5194/acp-10-11707-2010, 2010.

van Leeuwen, T. T., van der Werf, G. R., Hoffmann, A. A., Detmers, R. G., Rücker, G., French, N. H. F., Archibald, S., Carvalho Jr., J. A., Cook, G. D., de Groot, W. J., Hély, C., Kasischke, E. S., Kloster, S., McCarty, J. L., Pettinari, M. L., Savadogo, P., Alvarado, E. C., Boschetti, L., Manuri, S., Meyer, C. P., Siegert, F., Trollope, L. A., and Trollope, W. S. W.: Biomass burning fuel consumption rates: a field measurement database, Biogeosciences, 11, 7305–7329, doi:10.5194/bg-11-7305-2014, 2014.

Verma, M., Schimel, D., Evans, B., Frankenberg, C., Beringer, J., Drewry, D.T., Magney, T., Marang, I., Hutley, L., Moore, C. and Eldering, A. Effect of environmental conditions on the relationship between solar-induced fluorescence and gross primary productivity at an OzFlux grassland site. Journal of Geophysical Research: Biogeosciences, 122, 716-733, 2017.

Ward, D. E., Hao, W. M., Susott, R. A., Babbitt, R. E., Shea, R. W., Kauffman, J. B., & Justice, C. O.: Effect of fuel composition on combustion efficiency and emission factors for African savanna ecosystems. Journal of Geophysical Research: Atmospheres, 101, 23569-23576, 1996.

Wieder, W. R., Cleveland, C. C., Smith, W. K., and Todd- Brown, K. E. O.: Future productivity and carbon storage limited by terrestrial nutrient availability, Nat. Geosci., 8, 441–444, https://doi.org/10.1038/ngeo2413, 2015.

Williams, C.A. and Albertson, J.D: Soil moisture controls on canopy-scale water and carbon fluxes in an African savanna. Water Resources Research, 40, 2004.

Williams, M., Schwarz, P. A., Law, B. E., Irvine, J., and Kurpius, M. R.: An improved analysis of forest carbon dynamics using data assimilation, Glob. Change Biol., 11, 89–105, 2005.

Wolf, S., Keenan, T.F., Fisher, J.B., Baldocchi, D.D., Desai, A.R., Richardson, A.D., Scott, R.L., Law, B.E., Litvak, M.E., Brunsell, N.A., Peters, W., van der Laan-Luijk, I. T.: Warm spring reduced carbon cycle impact of the 2012 US summer drought. Proceedings of the National Academy of Sciences, 113, 5880-5885, 2016.

Worden, J.R., Bloom, A.A., Pandey, S., Jiang, Z., Worden, H.M., Walker, T.W., Houweling, S. and Röckmann, T.: Reduced biomass burning emissions reconcile conflicting estimates of the post-2006 atmospheric methane budget. Nature communications, 8, 2227, 2017.

Xu, X., Medvigy, D., Powers, J.S., Becknell, J.M. and Guan, K.: Diversity in plant hydraulic traits explains seasonal and inter-annual variations of vegetation dynamics in seasonally dry tropical forests. New Phytologist, 212, 80-95, 2016

Xu, T., Valocchi, A.J., Ye, M. and Liang, F.: Quantifying model structural error: Efficient Bayesian calibration of a regional groundwater flow model using surrogates and a data-driven error model. *Water Resources Research*, *53*(5), pp.4084-4105, 2017.

Yang, Y., Saatchi, S.S., Xu, L., Yu, Y., Choi, S., Phillips, N., Kennedy, R., Keller, M., Knyazikhin, Y. and Myneni, R.B.: Post-drought decline of the Amazon carbon sink. Nature communications, 9(1), p.3172, 2018.

Yin, Y., Bloom, A.A., Worden, J., Saatchi, S., Yang, Y., Williams, M., Liu, J., Jiang, Z., Worden, H., Bowman, K. and Frankenberg, C.: Fire decline in dry tropical ecosystems enhances decadal land carbon sink. Nature communications, 11(1), 1-7, 2020.

Zhang, Y., Joiner, J., Alemohammad, S.H., Zhou, S. and Gentine, P.: A global spatially contiguous solar-induced fluorescence (CSIF) dataset using neural networks. Biogeosciences, 15, 5779-5800, 2018.

Zhou, S., Yu, B., Huang, Y. and Wang, G.: Daily underlying water use efficiency for AmeriFlux sites. Journal of Geophysical Research: Biogeosciences, 120(5), pp.887-902, 2015.

Figures

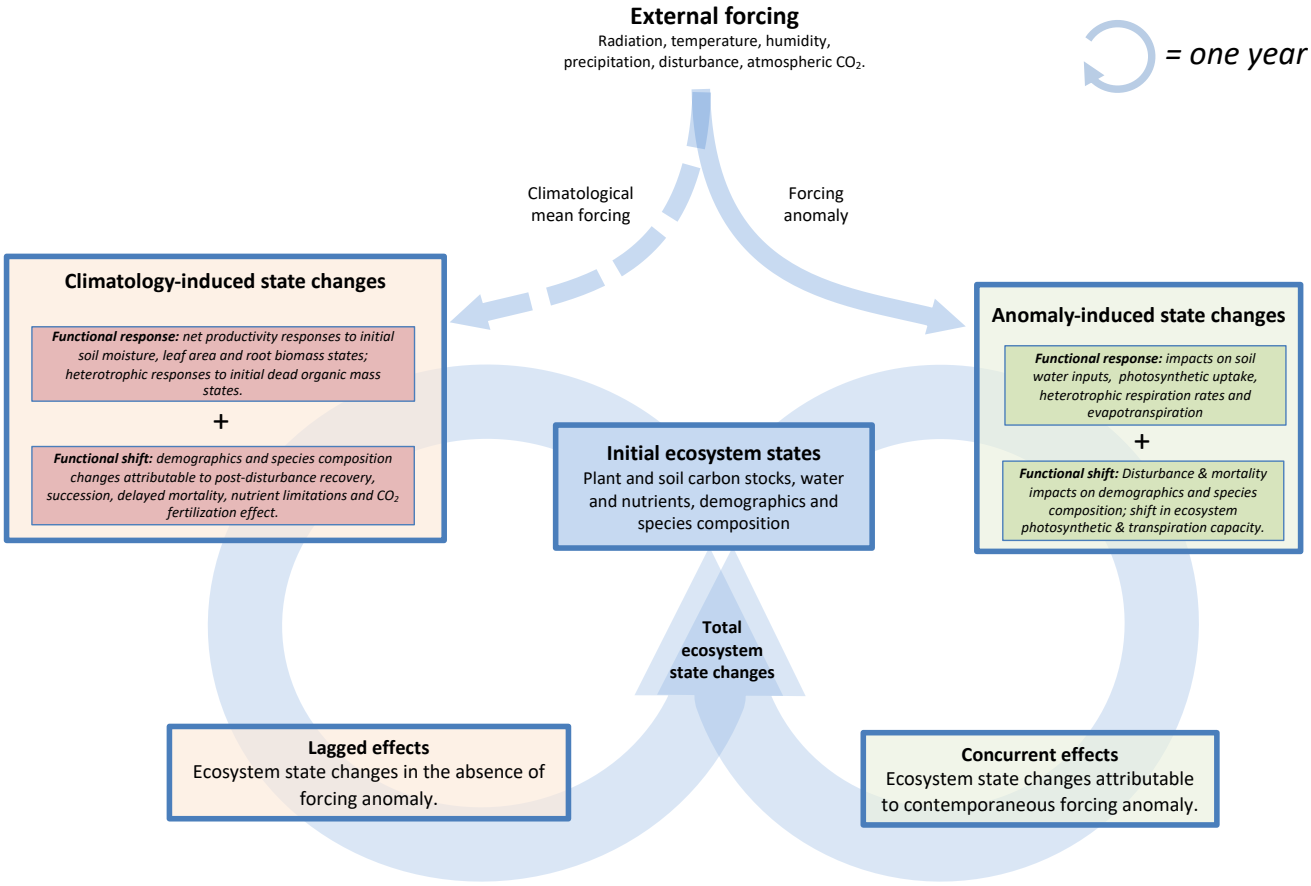

Figure 1. Conceptual figure denoting annual ecosystem states changes attributable to concurrent and lagged effects. Throughout a one-year cycle (circular arrows), lagged effects amount to the sum of ecosystem state changes induced by a reference climatological mean forcing, and concurrent effects amount ecosystem state changes solely attributable to a contemporaneous forcing anomaly. The total state changes resulting from both concurrent and lagged effects will in turn determine the next year's initial ecosystem states.

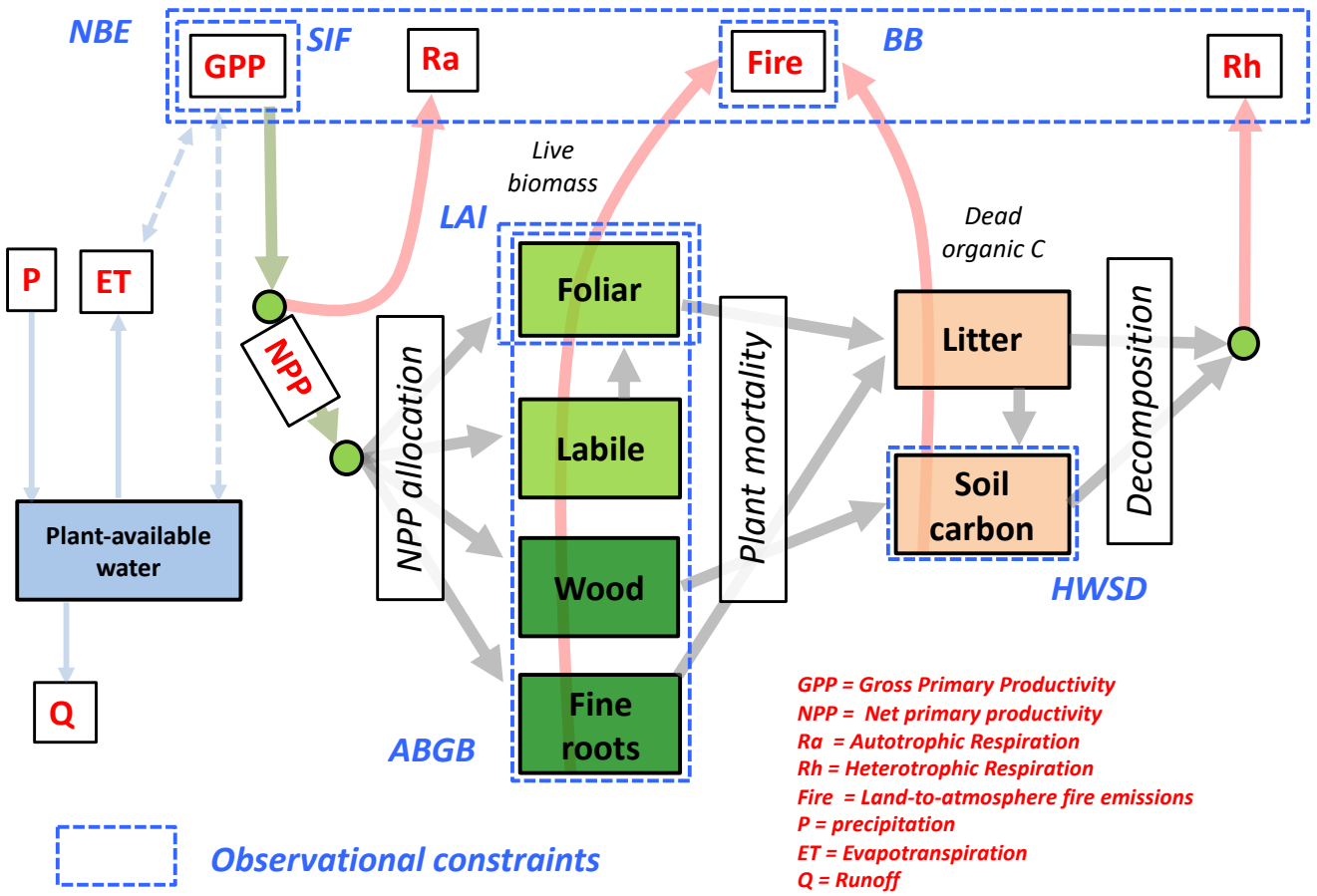

Figure 2. Schematic of the CARbon DAta-MOdel fraMework (CARDAMOM) Bayesian model-data fusion approach: the DALEC2a model (described in section 2.2) represents the ecosystem C and plant-available H_2O balance; the dashed blue boxes denote the observational constraints used in this study (see Table 1 for acronyms and details). The solid lines denote C and H_2O fluxes between pools and/or external gains and losses. CARDAMOM is implemented at a 4°×5° resolution across the tropics (30°S – 30°N). Within each 4°×5° grid cell, DALEC2a model parameters and initial ecosystem states are optimized using an adaptive Metropolis-Hastings Markov Chain Monte Carlo algorithm.

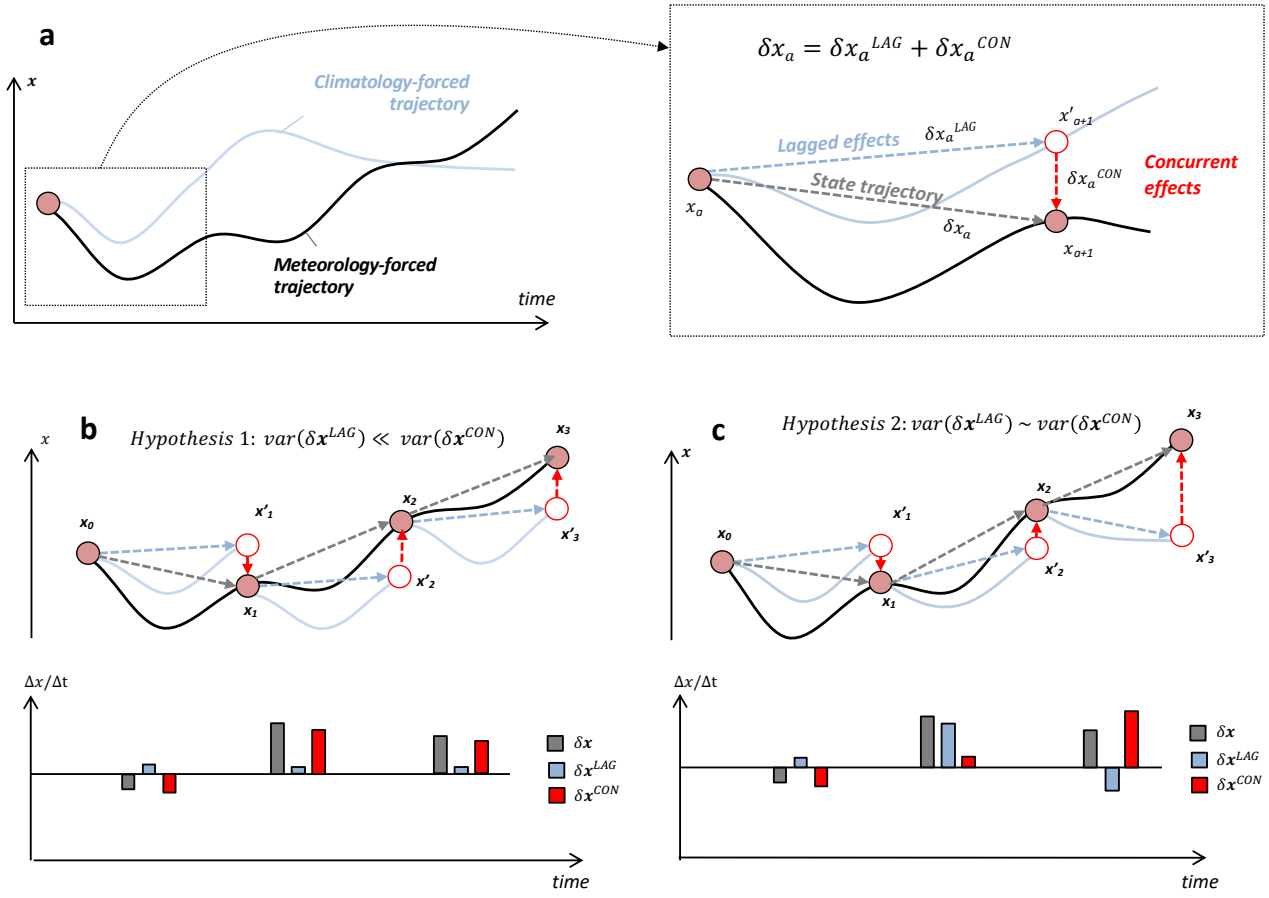

Figure 3. (**a**) Schematic of meteorology-forced trajectory of ecosystem state x (solid black line), and trajectory of x under a climatological mean forcing (light blue solid line). Inset: state trajectory $x_a \rightarrow x_{a+1}$ (δx_a), decomposed as the sum of climatology-induced lagged effect vector $x_a \rightarrow x'_{a+1}$ (δx_a^{LAG}) and anomaly-induced concurrent effect vector $x'_{a+1} \rightarrow x_{a+1}$ (δx_a^{CON}). (**b**) Hypothetical scenario depicting approximately time-invariant annual lagged effects $\delta \boldsymbol{x}^{LAG}$ (blue dashed arrows), in reference to changes transient states x_0, x_1, x_2, etc.; the temporal changes in x for each time interval, $\delta \boldsymbol{x}$ and $\delta \boldsymbol{x}^{LAG}$ and $\delta \boldsymbol{x}^{CON}$ are shown in the underlying bar chart. In this scenario, $\delta \boldsymbol{x}^{LAG}$ is relatively constant and its variability (denoted as "var()" in schematic equation) is negligible relative to $\delta \boldsymbol{x}^{CON}$. (**c**) Hypothetical scenario depicting time-varying annual lagged effects $\delta \boldsymbol{x}^{LAG}$, in reference to transient states $\boldsymbol{x_0}$, $\boldsymbol{x_1}$, $\boldsymbol{x_2}$, etc.; in this scenario, the variability of $\delta \boldsymbol{x}^{CON}$ is comparable to the variability of $\delta \boldsymbol{x}^{LAG}$.

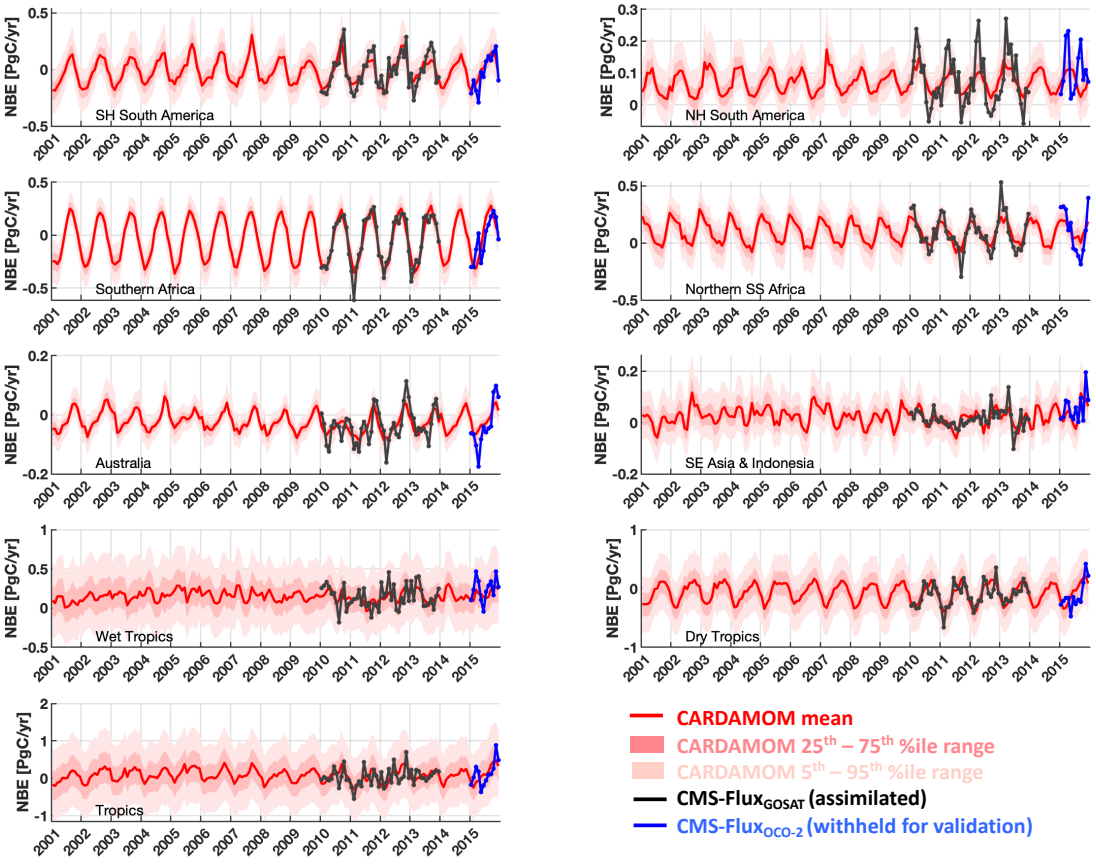

Figure 4. CARDAMOM monthly analyses of 2001-2015 median NBE (red line) and associated uncertainty intervals (25th-75th percentiles in dark pink, and 5th – 95th percentiles in light pink). The analyses were constrained by CMS-Flux GOSAT-derived top down fluxes (Liu et al., 2018) for the 2010-2013 period; CMS-Flux OCO-2 derived 2015 NBE fluxes were withheld for validation. The geographical definitions for each region are shown in Figure A1.

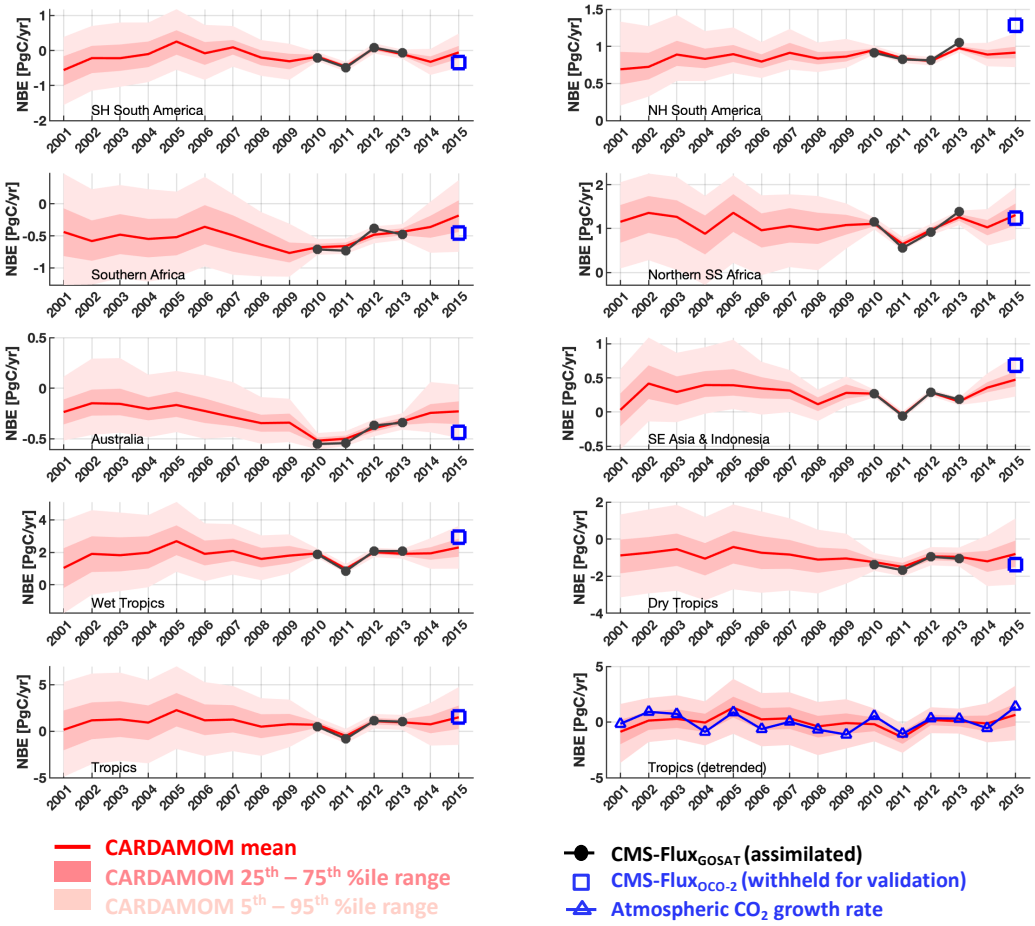

Figure 5. CARDAMOM yearly analyses of 2001-2015 NBE (red line) and associated uncertainty intervals (25^{th}-75^{th} percentiles in dark pink, and 5^{th} – 95^{th} percentiles in light pink). The analyses were constrained by CMS-Flux GOSAT-derived top down fluxes (Liu et al., 2018) for the 2010-2013 period. CMS-Flux OCO-2 derived 2015 NBE (blue squares) are withheld for regional and pan-tropical NBE validation. CARDAMOM NBE and NOAA ESRL atmospheric CO_2 growth rates were detrended for inter-comparison (bottom-right panel). The geographical definitions for each region are shown in Figure A1.

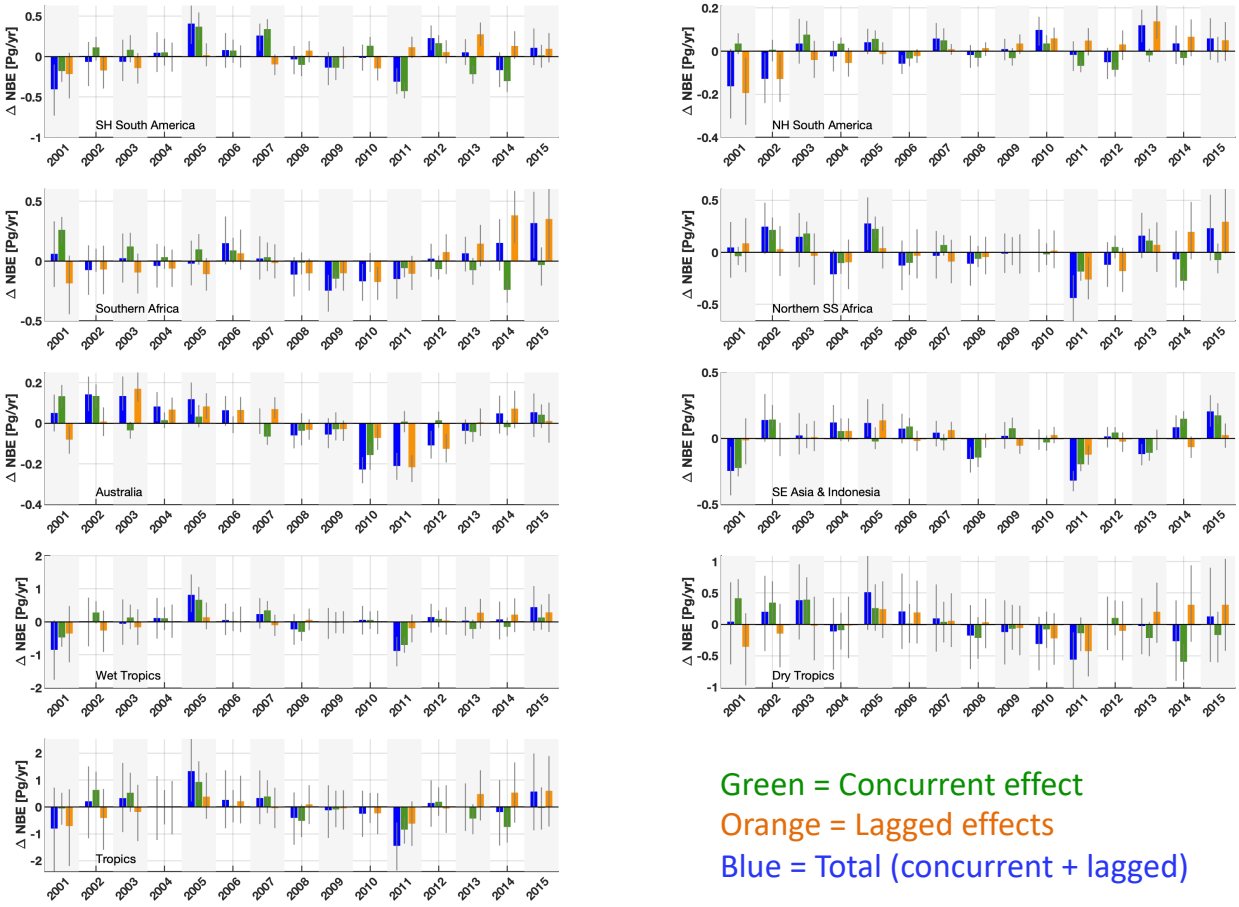

Figure 6. Regional and pan-tropical median annual ΔNBE (blue bars) and its attribution to concurrent effects (ΔNBE^{CON}, green bars) and lagged effect (ΔNBE^{LAG}, orange bars) components. The geographical definitions for each region are shown in Figure A1. Error bars denote the 25th – 75th percentile uncertainty estimates for each flux anomaly.

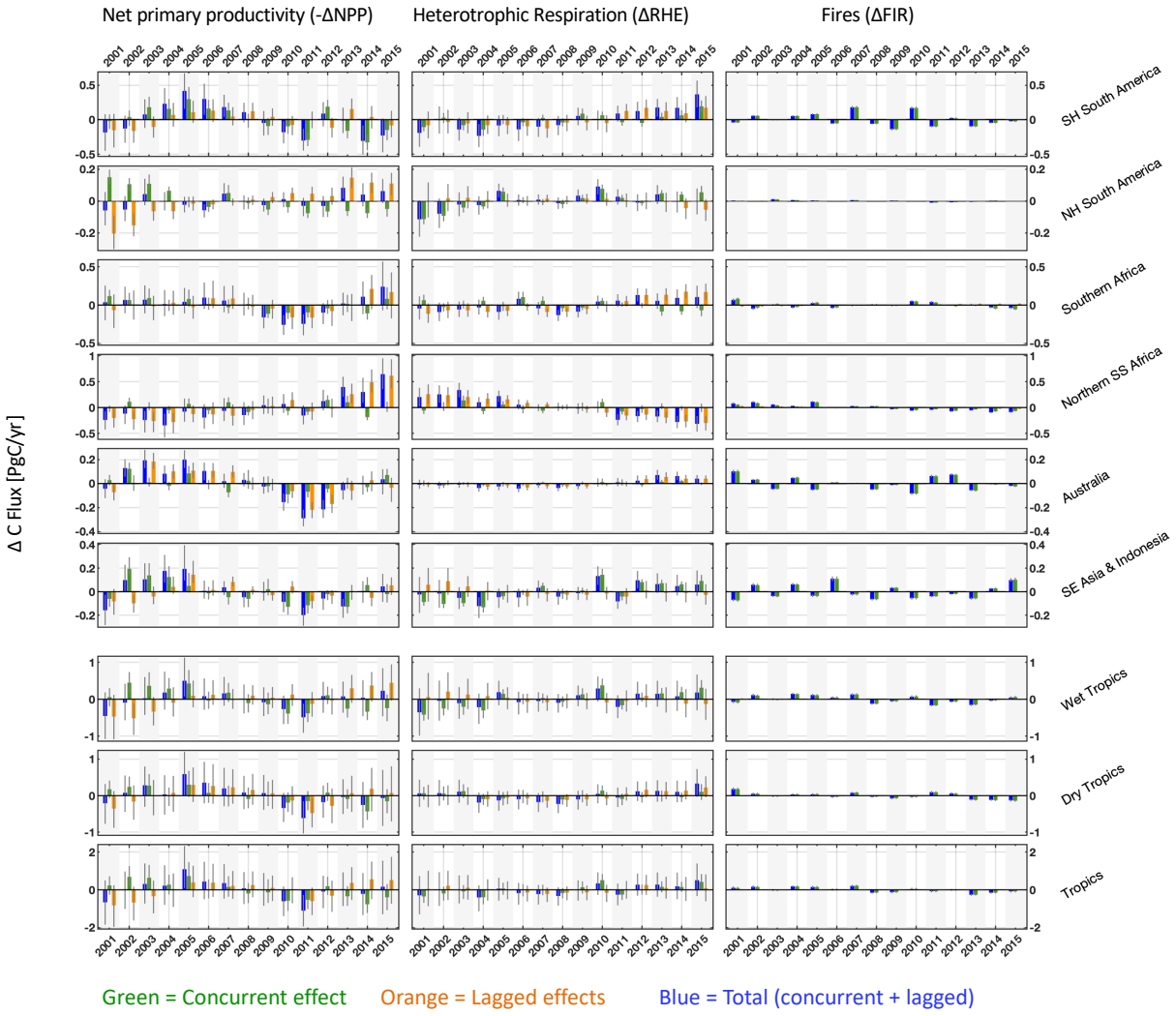

Figure 7. Regional and pan-tropical median annual net primary productivity (left column), heterotrophic respiration (center column) and fires (right column) anomalies (ΔNPP, ΔRHE and ΔFIR respectively). Blue bars represent total anomalies, green and orange bars represent the corresponding annual concurrent and lagged effects. ΔNPP anomaly signs were reversed such that all anomalies are represented as positive for net land-to-atmosphere C flux. The sum of annual ΔNPP, ΔRHE and ΔFIR are equivalent to annual ΔNBE values presented in Figure 6. Error bars denote the 25th – 75th percentile uncertainty estimates for each flux anomaly.

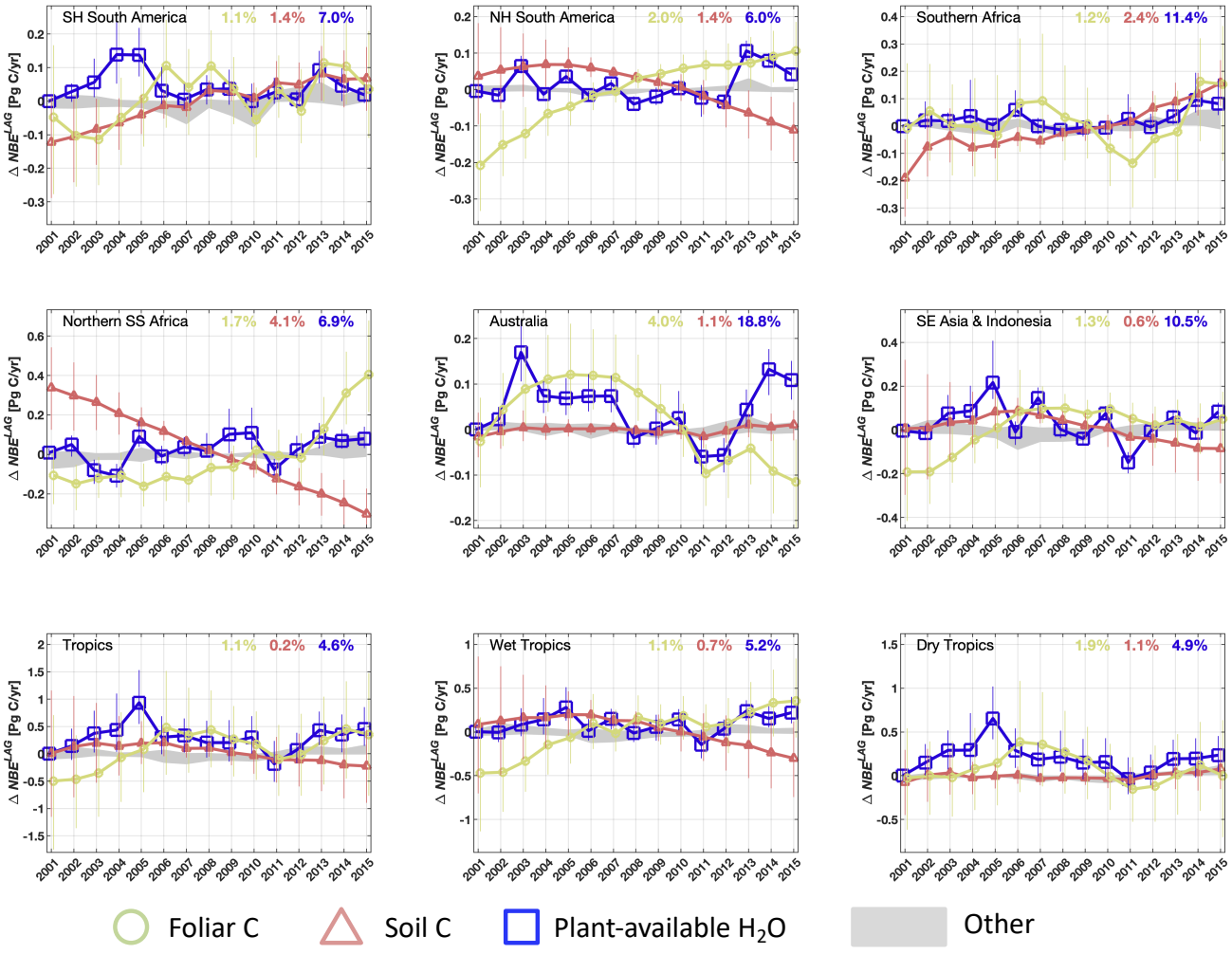

Figure 8: Attribution of 2001-2015 annual regional and pan-tropical NBE lagged effect estimates (ΔNBE^{LAG}) to individual ecosystem state anomalies (i.e. the lagged effect in year a solely attributable to anomaly in ecosystem state n, $\Delta NBE^{LAG}_{a(n)}$, see Eq. 22). In addition to foliar C (green circles), soil C (dark pink triangles), plant-available H_2O (blue squares), the grey areas (labelled as "Other" in the figure legend) denote the collective range of ΔNBE^{LAG} anomalies attributable to labile, wood, root and litter C. Percentage values indicate the inter-annual variability (reported as standard deviation) of median foliar C, soil C and plant-available H_2O states throughout the 2001-2015 period, relative to mean 2001-2015 values within each region. The sum of annual state-specific ΔNBE^{LAG} values is approximately equal to the ΔNBE^{LAG} (see Figure S4). Error bars denote the 25^{th} – 75^{th} percentile uncertainty estimates for each flux anomaly

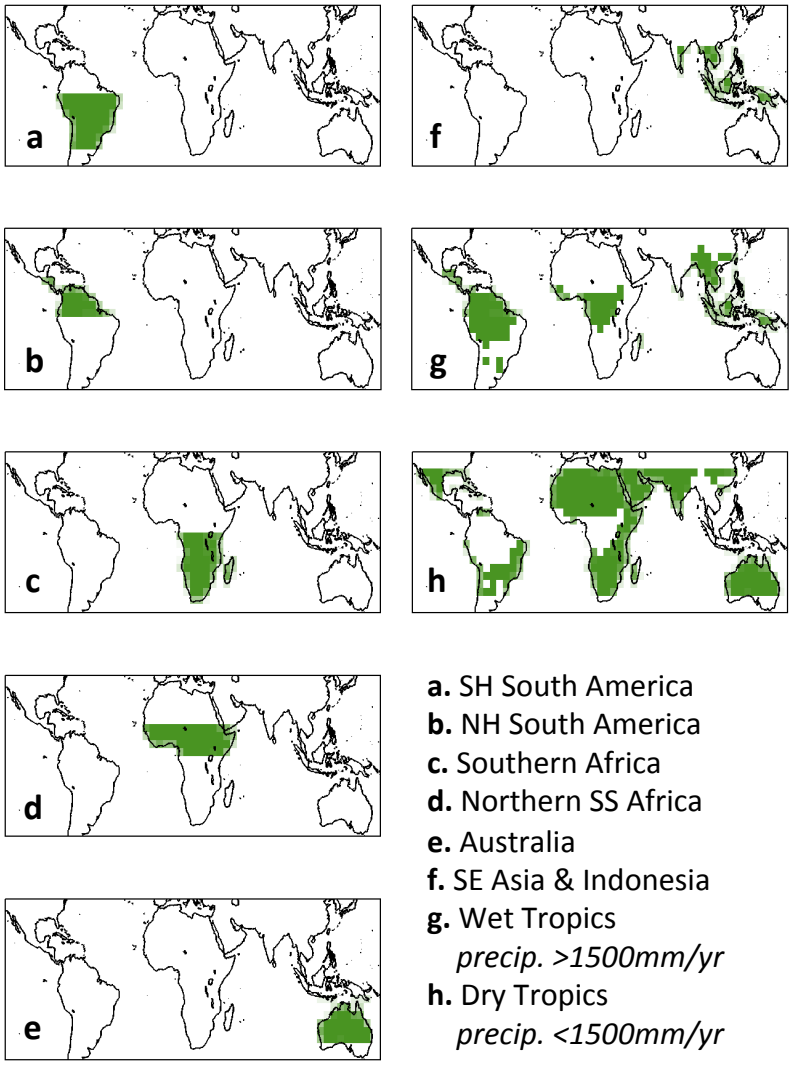

Figure A1. Regional masks used in this study. The 1500mm/yr precipitation thresholds were based on the ERA-interim mean annual precipitation rates throughout the 2001-2015 study period.

Tables

Table 1. Observational constraints assimilated into the 4°×5° CARDAMOM simulation.

Observation (acroynm)	Dataset description	Uncertainty[1]	Number of observational Constraints[6]
Leaf area index (LAI)	MODIS LAI retrievals[2].	±log(1.2)	1
Soil organic matter (SOM)	Soil C inventory (Hiederer & Kochy, 2011)	±log(1.5)	1
Above- and below-ground biomass (ABGB)[3]	GLAS-informed biomass map (Saatchi et al., 2011)	≥ ±log(1.5)[4]	1
Solar-induced Fluorescence (SIF)	Monthly averaged 2010-2015 GOSAT retrievals of fluorescence (Frankenberg et al., 2011)[5]	±log(2)	≤72
Fire C emissions (BB)	Mean 2001-2015 4°×5° inverse estimates of fire C emissions (Worden et al., 2017, Bowman et al., 2017).	±20%	1
Net Biospheric Exchange (NBE)	Monthly 2010-2013 GOSAT CO_2 derived 4°×5° inverse estimates of terrestrial NBE (Liu et al., 2018).	Seasonal = ±2gC/m^2/d Annual= ±0.02gC/m2/d	48

[1]Uncertainties denoted as ±log() indicate log-transformed model and observed quantities (i.e. *m* and *o* in Eq. 4).

[2]Only mean 2001-2015 LAI is assimilated into CARDAMOM, in order to mitigate the influence of seasonal LAI retrieval biases (Bi et al., 2015).

[3]The ABGB estimate is applied as a constraint on the sum of all CARDAMOM live biomass pools (Figure 1).

[4]see Bloom et al., 2016 for details on biomass uncertainties below.

[5]Time-resoved SIF is assimilated as a relative constraint on the temporal variability of GPP (see section 2.4).

[6]Figure S1 for observational constraint spatial coverage.

Table 2. CARDAMOM NBE evaluation against assimilated and predicted NBE

	Monthly RMSE[a] (Pearson's r)		Annual RMSE[a,b] (Pearson's r)	
	Assimilated NBE (2010-2013)	Predicted NBE (2015)	Assimilated NBE (2010-2013)	Predicted NBE (2015)
SH South America	0.08 (0.84*)	0.08 (0.87*)	0.03 (0.99*)	0.29 (-)
NH South America	0.06 (0.74*)	0.09 (-0.13)	0.04 (0.90)	0.37 (-)
Southern Africa	0.08 (0.94*)	0.13 (0.78*)	0.07 (0.92)	0.28 (-)
Northern SS Africa	0.08 (0.87*)	0.13 (0.96*)	0.08 (0.99*)	0.07 (-)
Australia	0.04 (0.69*)	0.05 (0.88*)	0.03 (0.98*)	0.21 (-)
SE Asia & Indonesia	0.03 (0.57*)	0.05 (0.55)	0.02 (0.99*)	0.21 (-)
Tropics	0.20 (0.51*)	0.27 (0.55)	0.19 (1.00*)	0.05 (-)
Wet Tropics	0.12 (0.58*)	0.14 (0.53)	0.12 (0.99*)	0.64 (-)
Dry Tropics	0.12 (0.80*)	0.20 (0.59*)	0.13 (0.99*)	0.58 (-)

[a]RMSE units are PgC/yr.

[b]Prediction RMSE values are equivalent to absolute errors, since only one error value is considered.

[*]Correlation p-value<0.05

Table 3. 2001-2015 regional Δ*NBE* IAV and corresponding contributions of concurrent effects (ΔNBE^{CON}) and lagged effects (ΔNBE^{LAG}); IAV values are represented here as standard deviations of annual 2001-2015 NBE values; bracketed values represent the Pearson's correlation coefficients between total NBE and concurrent and lagged effect IAV. The regional masks are depicted in Figure A1.

	Δ*NBE* IAV [Pg C/yr]	ΔNBE^{CON} IAV [as % of Δ*NBE* IAV] (Pearson's r)	ΔNBE^{LAG} IAV [as % of Δ*NBE* IAV] (Pearson's r)
SH South America	0.21	107%(0.81*)	63%(0.18)
NH South America	0.08	61%(0.16)	105%(0.83*)
Southern Africa	0.14	83%(0.10)	122%(0.76*)
Northern SS Africa	0.19	74%(0.70*)	71%(0.68*)
Australia	0.12	63%(0.56*)	84%(0.78*)
SE Asia & Indonesia	0.15	84%(0.91*)	41%(0.54*)
Wet Tropics	0.42	79%(0.89*)	45%(0.63*)
Dry Tropics	0.28	99%(0.65*)	83%(0.43)
Tropics	0.62	80%(0.76*)	64%(0.61*)

Table 4. Concurrent and lagged effect *NBE* attributed to constituent fluxes (net primary production, heterotrophic respiration and fires, abbreviated as *NPP*, *RHE* and *FIR* respectively): IAV values are represented here as the ratio of constituent flux standard deviation to *NBE* standard deviations of annual 2001-2015 *NBE* values; bracketed values corresponds to Pearson's correlation coefficients between constituent flux and *NBE* ("*" denotes p-values < 0.05). The values highlighted in red denote the largest % IAV contribution to ΔNBE^{CON} and ΔNBE^{LAG}.

	IAV as % of ΔNBE^{CON} (Pearson's r)			IAV as % of ΔNBE^{LAG} (Pearson's r)		
	ΔNPP^{CON}	ΔRHE^{CON}	ΔFIR^{CON}	ΔNPP^{LAG}	ΔRHE^{LAG}	ΔFIR^{LAG}
SH South America	**83%(-0.83*)**	38%(-0.46)	42%(-0.26)	**81%(-0.62*)**	78%(0.68*)	1%(0.15)
NH South America	**159%(-0.69*)**	115%(0.23)	11%(0.59*)	**116%(-0.98*)**	26%(-0.34)	1%(-0.91*)
Southern Africa	**66%(-0.74*)**	48%(-0.66*)	31%(-0.73*)	**61%(-0.79*)**	60%(0.83*)	7%(0.68*)
Northern SS Africa	**64%(-0.82*)**	43%(0.50)	38%(0.47)	**196%(-0.68*)**	136%(-0.24)	11%(-0.20)
Australia	**82%(-0.71*)**	15%(0.05)	74%(0.05)	**113%(-0.95*)**	29%(-0.16)	3%(-0.36)
SE Asia & Indonesia	**79%(-0.60*)**	67%(0.04)	49%(-0.09)	**112%(-0.80*)**	63%(0.15)	3%(0.32)
Wet Tropics	**87%(-0.64*)**	68%(0.24)	30%(0.21)	**147%(-0.93*)**	52%(-0.54*)	4%(-0.75*)
Dry Tropics	**73%(-0.93*)**	30%(-0.28)	33%(-0.39)	**102%(-0.86*)**	49%(0.25)	2%(0.18)
Tropics	**95%(-0.86*)**	52%(0.18)	28%(0.43)	**113%(-0.93*)**	35%(-0.05)	2%(-0.49)

Table 5. IAV of 2001-2015 regional and pan-tropical NBE lagged effects attributable to annual anomalies in column-denoted ecosystem states (Eq. 22), as % of total NBE lagged effects (ΔNBE^{LAG}) IAV; bracketed values correspond to Pearson's correlation coefficients between single-state NBE lagged effects and total ΔNBE^{LAG}; "*" denotes p-values < 0.05. The values highlighted in red denote the maximum contribution in each region.

	Labile C	Foliar C	Fine Root C	Wood C	Litter C	Soil C	Plant-av. H_2O
SH South America	9%(0.88*)	**48%(0.69*)**	15%(0.12)	2%(-0.80*)	27%(0.43)	41%(0.85*)	30%(0.28)
NH South America	3%(0.88*)	**98%(0.94*)**	6%(0.48)	6%(-0.91*)	12%(0.17)	34%(-0.17)	28%(0.45)
Southern Africa	6%(0.17)	**41%(0.69*)**	3%(0.66*)	1%(0.58*)	15%(0.85*)	40%(0.78*)	17%(0.85*)
Northern SS Africa	35%(0.45)	120%(0.64*)	2%(-0.01)	4%(-0.16)	12%(-0.03)	**125%(-0.22)**	50%(0.58*)
Australia	8%(0.71*)	**58%(0.68*)**	3%(-0.61*)	1%(-0.53*)	11%(-0.02)	10%(0.17)	54%(0.88*)
SE Asia & Indonesia	7%(0.14)	43%(0.16)	18%(-0.63*)	5%(0.29)	35%(0.07)	62%(0.45)	**64%(0.94*)**
Wet Tropics	8%(0.66*)	**99%(0.84*)**	14%(0.18)	8%(-0.73*)	27%(0.12)	56%(-0.55*)	37%(0.79*)
Dry Tropics	16%(0.71*)	**47%(0.70*)**	6%(-0.09)	1%(0.37)	17%(0.38)	13%(0.58*)	43%(0.83*)
Tropics	12%(0.82*)	**58%(0.83*)**	10%(0.03)	3%(-0.51)	21%(0.23)	20%(-0.26)	39%(0.82*)